



TECHNISCHE
UNIVERSITÄT
WIEN
Vienna University of Technology

Diplomarbeit

Investigation of the Relationship between Fe_2VAI -based Thin Films Sputtered on Silicon and their Bulk Analogon with Respect to the Thermoelectric Properties

Ausgeführt am Festkörperinstitut
der Technischen Universität Wien

unter der Anleitung von

Projektass. Dipl.-Ing. Alexander Riss
und

Ao.Univ.Prof. Dipl.-Ing. Dr.techn. Ernst Bauer

durch

Martin Stöger, BSc

SS 2021

Abstract

In this work, the thermoelectric properties of Heusler substrate-film systems are investigated based on $(\text{Fe}_{2/3}\text{V}_{1/3})_{75+x}\text{Al}_{25-x}$ compounds with $x = \{-4, -3, 3, 4\}$ and compared with their bulk analogs. Seebeck measurements of bulk samples show absolute values of up to $100 \mu\text{V K}^{-1}$, whereas annealed films on silicon substrates exhibit absolute values exceeding $600 \mu\text{V K}^{-1}$. To investigate this rise of S , measurements of silicon wafers are performed to quantify the influence of the substrate on the total Seebeck coefficient. Silicon wafers, which were produced using the Czochralski method, show a drop in resistivity after annealing, due to oxygen contamination during production of the wafers. Together with silicon's large Seebeck coefficient, this leads to a considerable contribution to the total measured Seebeck coefficient. For simplification purposes, aluminium, chromium and stoichiometric Fe_2VAl films are manufactured to showcase their behavior on silicon substrates. High absolute values of the Seebeck coefficients of about $500 \mu\text{V K}^{-1}$ are achieved, when using very thin films, which have no relevant Seebeck coefficient themselves. For the purpose of subsequently reducing the film's thickness, a sputter etching module is introduced into the sputtering device. Furthermore, a mathematical model to describe the angle- and distance-dependent sputtering rate is developed to increase the homogeneity of the film by optimization of the distance between sputter target and substrate.

Zusammenfassung

In dieser Arbeit werden die thermoelektrischen Eigenschaften von Heusler Substrat-Schicht Systemen, basierend auf der Verbindung $(\text{Fe}_{2/3}\text{V}_{1/3})_{75+x}\text{Al}_{25-x}$ mit $x = \{-4, -3, 3, 4\}$ untersucht und mit ihren Bulk Gegenstücken verglichen. Seebeck Messungen der Bulk Proben zeigen hohe Absolutwerte von bis zu $100 \mu\text{V K}^{-1}$, wohingegen die von wärmebehandelten Schichten auf Silizium Substraten $600 \mu\text{V K}^{-1}$ überschreiten. Um diesen Anstieg von S zu untersuchen, werden Siliziumwafer gemessen um deren Einfluss auf den totalen Seebeck Koeffizienten zu quantifizieren. Wärmebehandelte Siliziumwafer, die mittels Czochralskiverfahrens hergestellt wurden, weisen einen erniedrigten elektrischen spezifischen Widerstand auf, was auf Sauerstoffkontamination während des Herstellungsprozesses zurückzuführen ist. Mit dem hohen Seebeck Koeffizienten von Silizium führt dies zu einem nicht zu vernachlässigenden Beitrag zum gesamten Seebeck Koeffizienten. Zur Vereinfachung werden Aluminium-, Chrom- und stöchiometrische Fe_2VAl -Schichten hergestellt, um deren Eigenschaften auf Silizium Substraten zu beleuchten. Hohe Absolutwerte des Seebeck Koeffizienten von etwa $500 \mu\text{V K}^{-1}$ können bei sehr dünnen Schichten erreicht werden, die ihrerseits keinen relevanten Seebeck Koeffizienten vorweisen. Um die Schichtdicken anschließend verringern zu können, wird ein Sputterätzmodul in der Sputterkammer verbaut.

Außerdem wurde ein mathematisches Modell zur Beschreibung der winkel- und abstandsabhängigen Sputterrate entwickelt, um die Homogenität der Schichten durch Optimierung des Abstandes zwischen Sputtertarget und Substrat zu verbessern.

Contents

1	Basic Theoretical Concepts	6
1.1	Boltzmann Transport Equation	7
1.2	Transport Coefficients	9
1.3	Electrical Conductivity	10
1.4	Thermal Conductivity	11
1.5	Seebeck Effect	13
1.6	Peltier Effect	14
1.7	Thomson Effect	14
2	Thermoelectric Generators	15
2.1	Power Factor and Figure of Merit	16
2.2	Efficiency	16
3	Heusler Compounds	17
3.1	Fe ₂ VAI	18
4	X-ray Diffraction	21
4.1	X-ray Fluorescence	22
5	Sputtering	23
5.1	DC-Sputtering	23
5.2	RF-Sputtering	25
5.3	Magnetron Sputtering	25
5.4	Sputter Etching	25
5.5	Intensity Distribution	27
6	Material Synthesis	31
6.1	Thin Film Production	32
6.2	Etching	37
7	Thin Films	43
7.1	Substrate-Film System	43
7.1.1	Electrical Resistivity	43
7.1.2	Seebeck Coefficient	44
8	Measurements	46
9	Results	49
9.1	Bulk Measurements	49
9.2	Silicon Substrate	52

9.3	Thin Film Measurements	55
9.4	Scraped-off Film	57
9.5	Aluminium Films	60
9.6	Chromium Films	61
9.7	Fe ₂ VAl-Films	63
10	Conclusio	67
	APPENDIX	73
A	Data Processing	73
B	Intensity Distribution	74
C	XRF-Evaluation	78

1 Basic Theoretical Concepts

Contrary to theories regarding liquids and gases, solid state physics treats rigid matter which exhibits short-range as well as long-range order. This definition is softened by including quasicrystal and amorphous solids. In an ideal crystal, atoms arrange themselves on a periodic grid. The resulting lattice has great influence on the physical properties of the crystal, and a lot of effort is put into understanding and determining the crystal lattice.

To fully describe a crystal one has to consider about 10^{23} atoms in the solid. It is evident that direct computation fails to fulfill this task. Therefore, approximations are made to be able to describe its behavior. Two simplifications are assumed, the adiabatic and the harmonic approximation. The adiabatic approximation implies that electrons are fast enough to follow any displacement of their corresponding atomic core, so they can be assumed to always be in an equilibrium with respect to the core. This makes it possible to describe electron and lattice dynamics separately. The harmonic approximation assumes a harmonic potential of the atom around its lattice point, which is a good simplification for small displacements. Using these approximations, the movement and the interaction of the cores with each other can be treated as quantized lattice vibrations by introducing them as quasiparticles, the phonons. The electrons are perceived as Bloch waves in their respective energy bands, moving in the periodic potential generated by the atomic cores. Their momentum cannot be compared with free electrons, as Bloch waves are no eigenstates of the momentum operator. The wave vector \mathbf{k} can be seen as a crystal momentum in a periodic potential. [9]

Understanding transport phenomena is essential regarding thermoelectrics, as important physical properties, like electrical and thermal conductivity, can be described. Transport implies non-equilibrium and can be treated using a semiclassical model. The group velocity of a Bloch wave packet is given by

$$\mathbf{v}_n = \frac{1}{\hbar} \nabla_{\mathbf{k}} E_n(\mathbf{k}), \quad (1.1)$$

with the band index n being a constant, as no band-band transitions are allowed. \hbar is the reduced Planck constant and E_n is the energy of the wave packet. Equation 1.1 and

$$\hbar \frac{d\mathbf{k}}{dt} = \mathbf{F}(\mathbf{r}, t) = q [\mathbf{E}(\mathbf{r}, t) + \mathbf{v}_n(\mathbf{k}) \times \mathbf{B}(\mathbf{r}, t)] \quad (1.2)$$

are the equations of motion in the semiclassical model for a particle with the electric charge q in a specific energy band with index n in an external electrical field \mathbf{E} and magnetic field \mathbf{B} . Taking the time derivative of equation 1.1 and inserting equation 1.2

leads to

$$\frac{d\mathbf{v}_{n,i}(\mathbf{k})}{dt} = \frac{1}{\hbar^2} \frac{\partial^2 E_n(\mathbf{k})}{\partial k_i \partial k_j} F_j. \quad (1.3)$$

This equation has the form of the classical equation of motion $\dot{\mathbf{v}} = \mathbf{F}/m$. From this, an effective mass term can be identified [9]:

$$\left(\frac{1}{m^*} \right)_{ij} = \frac{1}{\hbar^2} \frac{\partial^2 E_n(\mathbf{k})}{\partial k_i \partial k_j} \quad (1.4)$$

1.1 Boltzmann Transport Equation

The Boltzmann transport equation describes the behavior of the distribution of charge carriers, which is driven by external forces, dissipation and scattering processes. The equilibrium distribution is given by the Fermi-Dirac equation

$$f_0(E) = \frac{1}{e^{\frac{E-\mu}{k_B T}} + 1} \quad (1.5)$$

with the chemical potential μ and the Boltzmann constant k_B . Under the influence of external forces and scattering, f_0 transits into the non-equilibrium distribution $f(\mathbf{r}, \mathbf{k}, t)$. Without scattering processes, an electron is subject to electromagnetic forces and follows the semiclassical equations of motion 1.1 and 1.2. Therefore, an electron moves from $\mathbf{r} - \mathbf{v}(\mathbf{k})dt$ to \mathbf{r} within the time dt and changes its momentum from $\mathbf{k} - \mathbf{F}/\hbar dt$ to \mathbf{k} . This leads to

$$f(\mathbf{r}, \mathbf{k}, t) = f(\mathbf{r} - \mathbf{v}dt, \mathbf{k} - \mathbf{F}/\hbar dt, t - dt), \quad (1.6)$$

which can be shown using Liouville's theorem [2]. Another term is added to include scattering events. It considers electrons not reaching the desired point in the phase space as well as those which wouldn't reach it normally but do so due to scattering events. Expanding equation 1.6 to first order and using this scattering term leads to

$$\frac{\partial f}{\partial t} = -\frac{\mathbf{F}}{\hbar} \nabla_{\mathbf{k}} f - \mathbf{v} \nabla_{\mathbf{r}} f + \left(\frac{\partial f}{\partial t} \right)_{\text{Scatt}} \quad (1.7)$$

The terms on the right can be identified as a force, a dissipation and a scattering term

$$\frac{\partial f}{\partial t} = \left(\frac{\partial f}{\partial t} \right)_{\text{Force}} + \left(\frac{\partial f}{\partial t} \right)_{\text{Diss}} + \left(\frac{\partial f}{\partial t} \right)_{\text{Scatt}} \quad (1.8)$$

The scattering term can be expressed by the product of the probability $W_{\mathbf{k},\mathbf{k}'}$ that an electron is scattered from a state $\psi_{\mathbf{k}}$ to another state $\psi_{\mathbf{k}'}$, and the occupation of these

states, which is given by

$$\left(\frac{\partial f(\mathbf{k})}{\partial t}\right)_{\text{Scatt}} = - \int \frac{d\mathbf{k}'}{(2\pi)^3} \{W_{\mathbf{k},\mathbf{k}'} f(\mathbf{k})[1 - f(\mathbf{k}')] - W_{\mathbf{k}',\mathbf{k}} f(\mathbf{k}')[1 - f(\mathbf{k})]\} . \quad (1.9)$$

The two terms in the integrand treat scattering to and from the desired states. Solving equation 1.6 with a scattering term as seen in equation 1.9 is a difficult task. Therefore, the scattering term is often approximated by a simpler expression. This is achieved by introducing the relaxation time τ , which represents the mean time between two scattering events.

$$\left(\frac{\partial f}{\partial t}\right)_{\text{Scatt}} = - \frac{f(\mathbf{k}) - f_0(\mathbf{k})}{\tau(\mathbf{k})} \quad (1.10)$$

Equation 1.10 states that the non-equilibrium distribution is reverted to thermal equilibrium by scattering events. If a system is in a non-equilibrium state $f(\mathbf{k}, 0)$ at $t = 0$ and external forces are switched off, scattering events reduce the difference between $f(\mathbf{k}, 0)$ and $f_0(\mathbf{k})$ according to

$$f(\mathbf{k}, t) - f_0(\mathbf{k}) = (f(\mathbf{k}, 0) - f_0(\mathbf{k})) e^{-t/\tau} \quad (1.11)$$

To calculate the non-equilibrium distribution using the relaxation time approximation, one considers the number of electrons dN in the band with index n which are inside the volume $d\mathbf{r}d\mathbf{k}$ in the phase space at the time t .

$$dN = f_n(\mathbf{r}, \mathbf{k}, t) \frac{d\mathbf{r}d\mathbf{k}}{4\pi^3} \quad (1.12)$$

With the relaxation time ansatz, one can calculate the electrons which reach this volume at time t by following the semiclassical equations of motion after their last collision at time t' . Only a portion of these electrons reaches the volume, as the others are scattered. This part is defined as $P(t, t')$, which is given in equation 1.13.

$$P(t, t') = \exp\left(- \int_{t'}^t \frac{dt^*}{\tau(t^*)}\right) \quad (1.13)$$

By comparing equation 1.12 with the number of electrons reaching this volume, one can calculate the non-equilibrium distribution

$$f(t) = \int_{-\infty}^t \frac{dt'}{\tau(t')} f_0(t') P(t, t') . \quad (1.14)$$

Using the properties of $P(t, t')$ and inserting the semiclassical equation of motion, the

non-equilibrium distribution can be written as

$$f(t) = f_0 + \int_{-\infty}^t dt' P(t, t') \left[\left(-\frac{\partial f}{\partial E} \right) \mathbf{v} \left(-e\mathbf{E} - \nabla_r \mu - \left(\frac{E - \mu}{T} \right) \nabla_r T \right) \right]. \quad (1.15)$$

Note that a magnetic field term does not appear explicitly as the velocity is perpendicular to the Lorentz force [2].

1.2 Transport Coefficients

For weak, homogeneous electric fields and temperature gradients as well as for a location and energy-independent relaxation time, $P(t, t')$ becomes

$$P(t, t') = e^{-(t-t')/\tau_n(\mathbf{k})} \quad (1.16)$$

After inserting equation 1.16 in equation 1.15, the integral can be evaluated if there is no magnetic field present, leading to

$$\begin{aligned} f(\mathbf{k}) &= f_0 + \left(\frac{df}{dE} \right) \tau(\mathbf{k}) \mathbf{v}(\mathbf{k}) \cdot \left[e\mathbf{E} - \nabla_r \mu - \frac{E - \mu}{T} \nabla_r T \right] \\ &= f_0 + \left(\frac{df}{dE} \right) \tau(\mathbf{k}) \mathbf{v}(\mathbf{k}) \cdot \mathcal{A}. \end{aligned} \quad (1.17)$$

The electrical current density can be calculated by

$$\mathbf{j}_e = -\frac{e}{4\pi^3} \int \mathbf{v}(\mathbf{k}) f(\mathbf{k}) d^3k. \quad (1.18)$$

Inserting equation 1.17 in equation 1.18, one can find the following expression.

$$\mathbf{j}_e = \frac{1}{4\pi^3} \frac{e^2}{\hbar} \int dS_F \frac{\tau \mathbf{v} \mathbf{v}}{v} \cdot \left[\mathbf{E} - \frac{\nabla_r \mu}{e} \right] + \frac{1}{4\pi^3} \frac{e}{\hbar} \int dS_F \frac{\tau \mathbf{v} \mathbf{v}}{v} \cdot \frac{E - \mu}{T} [-\nabla_r T] \quad (1.19)$$

In the same manner the heat flux density is given by

$$\begin{aligned} \mathbf{j}_h &= \frac{1}{4\pi^3 \hbar} \int [E(\mathbf{k}) - \mu] \nabla_{\mathbf{k}} E(\mathbf{k}) f(\mathbf{k}) d^3k \\ &= \frac{1}{4\pi^3} \int [E(\mathbf{k}) - \mu] \mathbf{v}_{\mathbf{k}} f(\mathbf{k}) d^3k \end{aligned} \quad (1.20)$$

into which the non-equilibrium distribution from equation 1.17 is again inserted.

$$\begin{aligned} \mathbf{j}_h = & \frac{1}{4\pi^3\hbar} \iint dS_E dE \frac{[E(\mathbf{k}) - \mu]\tau(\mathbf{k})\mathbf{v}_k\mathbf{v}_k}{v_k} \left(-\frac{\partial f_0}{\partial E} \right) [e\mathbf{E} - \nabla_r\mu] \\ & + \frac{1}{4\pi^3\hbar} \iint dS_E dE \frac{[E(\mathbf{k}) - \mu]\tau(\mathbf{k})\mathbf{v}_k\mathbf{v}_k}{v_k} \left(-\frac{\partial f_0}{\partial E} \right) \left[\frac{E(\mathbf{k}) - \mu}{T} (-\nabla_r T) \right] \end{aligned} \quad (1.21)$$

Comparing equation 1.20 and 1.21, one can introduce the factors L^{ij} to identify the general transport equations

$$\mathbf{j}_e = L^{11}\mathbf{E} + L^{12}\left(-\frac{\nabla T}{T}\right) \quad (1.22)$$

$$\mathbf{j}_h = L^{21}\mathbf{E} + L^{22}\left(-\frac{\nabla T}{T}\right). \quad (1.23)$$

Rearrangement leads to a depiction in which it is obvious that an electric current and a temperature gradient produce an electric field as well as thermal flux.

$$\mathbf{E} = \rho\mathbf{j}_e + S\nabla T \quad (1.24)$$

$$\mathbf{j}_h = \Pi\mathbf{j}_e - \kappa\nabla T \quad (1.25)$$

The variables ρ , κ , Π and S are the common symbols of electrical resistivity, thermal conductivity, Peltier coefficient and Seebeck coefficient, respectively [9].

1.3 Electrical Conductivity

Electrical conductivity σ is a physical property, which links electrical current \mathbf{j}_e to an electric field \mathbf{E} according to Ohm's law

$$\mathbf{j}_e = \sigma\mathbf{E} = \frac{\mathbf{E}}{\rho}, \quad (1.26)$$

with the electrical resistivity $\rho = 1/\sigma$. In classical physics, the electrical conductivity of a free electron gas is determined by

$$\sigma = \frac{ne^2\tau}{m} = n|e|\mu \quad (1.27)$$

with the charge carrier density n , the relaxation time τ , the electron mass m , the electric charge e and the mobility $\mu = \frac{|e|\tau}{m}$.

Using the semiclassical model and comparing equations 1.22 and 1.26 at a constant

temperature, the conductivity tensor $\sigma_{\mu\nu}$ can be identified.

$$\sigma_{\mu\nu} = \frac{e^2}{4\pi^3\hbar} \int_{E=E_f} dS_E \frac{\tau v_\mu v_\nu}{v} \quad (1.28)$$

It is notable that in the semiclassical model, filled as well as empty bands don't influence electric current. Only partially filled bands take part in transport. With only one electron missing, the only empty state can be seen as a positive charge carrier with negative momentum, energy and effective mass compared to its electron counterpart. This positive quasiparticle is called electron hole. Current can thereby be distinguished as being driven by electrons or by electron holes.

The electric field and the current don't have to be parallel as the conductivity is a tensor depending on the crystal structure. In a crystal with cubic symmetry, however, $\sigma_{\mu\nu}$ is diagonal and \mathbf{E} and \mathbf{j}_e are aligned. In case of the effective mass m^* being independent of \mathbf{k} for all energy levels in a band, the classic expression from equation 1.27 can be found again [9]

$$\sigma_{\mu\nu} = \frac{ne^2\tau}{m_{\mu\nu}^*} . \quad (1.29)$$

1.4 Thermal Conductivity

A temperature difference in a solid will decrease over time, as heat will flow in the opposite direction of the temperature gradient. The thermal flux is given by

$$\mathbf{j}_h = -\kappa\nabla T . \quad (1.30)$$

In a solid, heat is transported by electrons, having more energy going from hot to cold than vice versa and by lattice vibrations, which transport energy via phonons. The total thermal conductivity is the sum of the electronic and the lattice conductivity.

$$\kappa = \kappa_e + \kappa_l \quad (1.31)$$

The electronic part κ_e can be expressed, as was the electrical conductivity, by the general transport coefficients L^{ij} from equations 1.22 and 1.23. Thereby the relation of thermal flux \mathbf{j}_h and a temperature gradient ∇T for $\mathbf{j}_e = 0$ is given using equation 1.25

$$\mathbf{j}_h = -\kappa_e\nabla T = [L^{22} - L^{21}(L^{11})^{-1}L^{12}](-\frac{\nabla T}{T}) \quad (1.32)$$

The second term in equation 1.32 is orders of magnitude smaller than the first term for metals, so it can be neglected. By the use of the Sommerfeld expansion, L^{22} can

be evaluated

$$\kappa_e = \frac{L^2}{T} = \frac{\pi^2}{3} \frac{k_B^2 T}{e^2} \sigma . \quad (1.33)$$

This is the Wiedemann-Franz law, which states that the ratio of thermal to electrical conductivity is constant for a given temperature.

The lattice contribution to the thermal conductivity κ_l can be derived from the kinetic theory of gases

$$\kappa_l = \frac{1}{3} c_V c l \quad (1.34)$$

with the heat capacity c_V and the mean free path $l = c\tau$. κ_l is determined by scattering of phonons on static imperfections, as well as by phonon scattering events called normal and Umklapp processes. The former keep the total crystal momentum constant and only the latter can change the momentum. At low temperatures, Umklapp processes are rather unlikely and only geometry and impurities influence the conductivity. The mean free path then rises exponentially until it is limited by the solid's boundaries. Therefore l becomes temperature independent and κ_l has the same temperature dependence as the heat capacity

$$\kappa_l \propto T^3 . \quad (1.35)$$

At temperatures higher than the Debye temperature θ_D , Umklapp processes rise exponentially and the lattice thermal conductivity falls again

$$\kappa_l \propto T^{-x} \quad (1.36)$$

with $1 < x < 2$, [2, 9].

A more general expression for the lattice conductivity is given by the Callaway function

$$\kappa_l = \frac{k_B}{2\pi^2 v_S} \left(\frac{k_B T}{\hbar} \right)^3 \int_0^{\theta_D/T} \tau \frac{x^4 e^x}{(e^x - 1)^2} dx + \kappa_2 , \quad (1.37)$$

with the Debeye temperature Θ_D and the relaxation time τ . The second term in the Callaway function κ_2 is dominant for a pure crystal, but becomes negligible when defects and impurities are present. Therefore the exact expression is not given at this point. The inverse of τ can be seen as a scattering rate. Normal (N)- and Umklapp (U)-processes, scattering by point defects (PD), electron-phonon scattering (EP) and boundary scattering (B) contribute to a combined scattering rate τ^{-1} , which can be calculated using Matthiessen's law [16]

$$\frac{1}{\tau} = \frac{1}{\tau_N} + \frac{1}{\tau_U} + \frac{1}{\tau_{PD}} + \frac{1}{\tau_{EP}} + \frac{1}{\tau_B} . \quad (1.38)$$

1.5 Seebeck Effect

Given a rod with an applied temperature gradient, an electric field will emerge inside it according to

$$\mathbf{E} = S\nabla T . \quad (1.39)$$

This mechanism is called the Seebeck effect, with the material-dependent Seebeck coefficient S . This can be visualized by imagining the charge carriers on the hot side having higher kinetic energies than the ones on the cold side. As a result, a net velocity to the cold side remains. As the electrons move from their equilibrium distribution, a charge excess on the cold side generates the electric field which grows up to the point where it compensates the electron flux. A popular application is the thermocouple. It consists of two conductors, A and B , which are connected at a junction and by a voltmeter. If the junction is held at T_1 and the other ends at T_2 , a voltage can be measured, which is proportional to the temperature difference [4].

$$U = \int \mathbf{E} d\mathbf{s} = \int_{T_1}^{T_2} (S_A - S_B) dT . \quad (1.40)$$

For constant Seebeck coefficients equation 1.40 becomes

$$U = (S_A - S_B)\Delta T . \quad (1.41)$$

Determining the absolute Seebeck coefficient is not simple, as only the difference of two materials can be measured. To circumvent this problem, one sample can be exchanged for a superconductor, for which $S = 0$ holds. Another possibility is to calculate S after measuring the Thomson effect, which is discussed in section 1.7, [2, 16].

The Seebeck coefficient itself can be determined by using the general transport coefficients obtained in section 1.2

$$\mathbf{E} = S\nabla T = (L^{11})^{-1}L^{12}\left(\frac{\nabla T}{T}\right) \quad (1.42)$$

$$S = \frac{(L^{11})^{-1}L^{12}}{T} = \frac{\pi^2 k_B^2 T}{3} \frac{\sigma'}{e \sigma} = \frac{\pi^2 k_B^2 T}{3} \frac{1}{e} \left[\frac{\partial \ln(\sigma)}{\partial E} \right]_{E=E_F} . \quad (1.43)$$

Assuming the electrical conductivity from equation 1.27, the Seebeck coefficient can be written as

$$S = \frac{\pi^2 k_B^2 T}{3} \frac{1}{e} \left[\frac{1}{D(E)} \frac{\partial D(E)}{\partial E} + \frac{\partial \ln(\mu(E))}{\partial E} \right]_{E=E_F} \quad (1.44)$$

with the density of states $D(E) = \frac{\partial n}{\partial E}$. For energy independent relaxation time τ , the

second term vanishes, which leads to the well known Mott's formula [9]

$$S(T) = \frac{\pi^2 k_B^2 T}{3 e} \left[\frac{D(E)}{n} \right]_{E=E_F} . \quad (1.45)$$

1.6 Peltier Effect

The reverse phenomenon of the Seebeck effect is the Peltier effect. If the voltmeter is replaced by a battery in the experiment from section 1.5, an electrical current flows through the conductors A and B . The Peltier effect states that one junction heats up while the other one cools down due to charge carriers transferring heat [4]. The rate of heat flow is dependent on the Peltier coefficient \dot{Q}

$$\dot{Q}_{Peltier} = (\Pi_A - \Pi_B)I . \quad (1.46)$$

As the Seebeck effect can be used to generate voltage from a temperature difference, the opposite can be achieved by the Peltier effect, which is used in applications for refrigeration.

1.7 Thomson Effect

The third thermoelectric property is the Thomson effect. If a current passes through a wire with an applied temperature gradient, heat is either absorbed or released along the wire due to the Thomson effect

$$\dot{Q}_{Thomson} = -\tau_{AB}I\nabla T \quad (1.47)$$

with the Thomson coefficient τ_{AB} [16].

This may not be confused with Joule heating inside the wire. Thomson heating is a reversible process and changes its sign with the current.

The three thermoelectric effects are related by the Thomson relations [16]

$$\Pi_{AB} = S_{AB}T \quad (1.48)$$

$$\tau_{AB} = T \frac{dS_{AB}}{dT} \quad (1.49)$$

$$\dot{Q}_{Peltier} = S_{AB}TI . \quad (1.50)$$

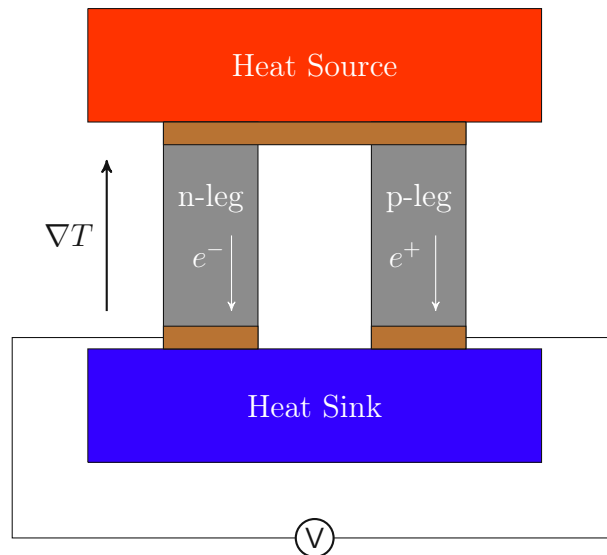


Figure 2.1. Model of a thermoelectric generator (TEG). A temperature gradient-driven current flows through the n-type and p-type thermoelectric legs, based on [25].

2 Thermoelectric Generators

A thermoelectric generator (TEG) is a heat engine, which uses a temperature gradient to convert heat into electric power by making use of the Seebeck effect. As energy efficiency is paramount in many of today's applications, especially regarding the rise of renewable energies, the possibility to recover waste heat is of great importance. Advantages of TEGs over other heat engines are the absence of moving parts, which reduces its susceptibility to errors, as well as the ability to scale it to different geometries. One of the first practical applications was the use of Radioisotope Powered Thermoelectric Generators (RTG), which are used as a power source in spacecrafts. It consists of a radioisotope which provides the heat for a TEG. In this kind of application, the total reliability outweighs the low efficiency. The challenge today is to push the efficiency, while still considering factors like weight, toxicity of used materials and costs [26].

A typical thermoelectric device consists of two legs, an n- and a p-conductor, which are connected electronically in series and thermally in parallel. Figure 2.1 shows a model of a TEG with a temperature gradient between heat source and heat sink. The Seebeck effect affects the primary charge carriers, which are electrons in case of n-type conductors and electron holes for p-type materials. Therefore, the Seebeck voltages of both legs add up according to equation 1.42, which can be measured by a voltmeter. As these devices usually don't produce enough voltage for typical applications, many of them are put together to form a battery [3].

2.1 Power Factor and Figure of Merit

Good thermoelectric materials are characterized by not only a high Seebeck coefficient but also by high electrical conductivity and low thermal conductivity. This relation is denoted by the figure of merit Z , which is often multiplied by the absolute temperature to get a dimensionless value ZT

$$ZT = \frac{S^2\sigma}{\kappa}T, \quad (2.1)$$

where $S^2\sigma$ is called the power factor. For practical purposes, ZT of thermoelectric materials should exceed 1 to get a conversion efficiency $\eta \geq 10\%$ [6]. Improving the figure of merit is not easy, as the predominant contributing terms are not independent of each other. To reduce thermal conductivity, for example, one has to focus on the lattice part, as electronic mobility is important for electrical conductivity, too. Different approaches to improve ZT include doping, band engineering and using size effects.

2.2 Efficiency

The efficiency of a thermoelectric generator is defined as [26]

$$\eta = \frac{\text{electric energy output}}{\text{thermal energy input at hot side}}, \quad (2.2)$$

which has the Carnot cycle efficiency as a theoretical maximum.

$$\eta_{Carnot} = \frac{T_H - T_C}{T_H} \quad (2.3)$$

T_H and T_C are the temperatures at the hot and the cold end, respectively.

For a TEG, η is given by

$$\eta = \frac{T_H - T_C}{T_H} \frac{\sqrt{1 + ZT_M} - 1}{\sqrt{1 + ZT_M} + T_C/T_H} \quad (2.4)$$

with T_M representing the mean temperature. Conversion efficiencies of 5% – 20% have been reported, with ongoing efforts to further increase ZT [6].

When using a thermoelectric device in refrigerator applications, the coefficient of performance CP is given by [25]

$$CP = \frac{T_C \left[\sqrt{1 + ZT_M} - T_H/T_C \right]}{(T_H - T_C) \left[\sqrt{1 + ZT_M} + 1 \right]}. \quad (2.5)$$

X_2YZ Heusler compounds

H 2.20																	He	
Li 0.98	Be 1.57											B 2.04	C 2.55	N 3.04	O 3.44	F 3.98	Ne	
Na 0.93	Mg 1.31											Al 1.61	Si 1.90	P 2.19	S 2.58	Cl 3.16	Ar	
K 0.82	Ca 1.00	Sc 1.36	Ti 1.54	V 1.63	Cr 1.66	Mn 1.55	Fe 1.83	Co 1.88	Ni 1.91	Cu 1.90	Zn 1.65	Ga 1.81	Ge 2.01	As 2.18	Se 2.55	Br 2.96	Kr 3.00	
Rb 0.82	Sr 0.95	Y 1.22	Zr 1.33	Nb 1.60	Mo 2.16	Tc 1.90	Ru 2.20	Rh 2.28	Pd 2.20	Ag 1.93	Cd 1.69	In 1.78	Sn 1.96	Sb 2.05	Te 2.10	I 2.66	Xe 2.60	
Cs 0.79	Ba 0.89		Hf 1.30	Ta 1.50	W 1.70	Re 1.90	Os 2.20	Ir 2.20	Pt 2.20	Au 2.40	Hg 1.90	Tl 1.80	Pb 1.80	Bi 1.90	Po 2.00	At 2.20	Rn	
Fr 0.70	Ra 0.90																	
		La 1.10	Ce 1.12	Pr 1.13	Nd 1.14	Pm 1.13	Sm 1.17	Eu 1.20	Gd 1.20	Tb 1.10	Dy 1.22	Ho 1.23	Er 1.24	Tm 1.25	Yb 1.10	Lu 1.27		
		Ac 1.10	Th 1.30	Pa 1.50	U 1.70	Np 1.30	Pu 1.28	Am 1.13	Cm 1.28	Bk 1.30	Cf 1.30	Es 1.30	Fm 1.30	Md 1.30	No 1.30	Lr 1.30		

Figure 3.1. Periodic table highlighting the elements used for Heusler compounds [7].

3 Heusler Compounds

Heusler compounds, discovered by Fritz Heusler [11], are a family of intermetallic materials, consisting of a 2:1:1 composition. Another group with a 1:1:1 composition is called Half-Heusler materials [7]. In thermoelectrics they are frequently used, because of their remarkable properties, many of which can be predicted by their valence electron count. Heusler compounds have the formula X_2YZ . X is a transition elements and Z is a main group element. Y is a transition element but can sometimes be replaced by a rare earth or an alkaline earth element. Figure 3.1 highlights the possible Heusler elements in the periodic table.

The crystal structure of Heusler compounds consists of four interpenetrating fcc-sublattices. This corresponds to the cubic space group $Fm\bar{3}m$ with the prototype Cu_2MnAl ($L2_1$). The X atoms occupy the Wyckoff position $8c$ ($1/4, 1/4, 1/4$), the Y and the Z atoms are located at $4a$ ($0, 0, 0$) and $4b$ ($1/2, 1/2, 1/2$), respectively [7].

Disorder has great effect on the physical properties of Heusler compounds. If Y and Z atoms occupy the same positions interchangeably, the crystal forms a CsCl-type structure called $B2$ disorder. If all elements are evenly distributed, tungsten-type disorder emerges ($A2$). Other possible disorder types are BiF_3 - and NaTl -type. To determine the existing type of crystal structure, mostly x-ray diffraction is used. By measuring the intensity and the angle of reflected x-ray beams, the lattice parameter and the purity of the desired structure can be assessed.

Oftentimes, Heusler compounds' physical properties can be predicted from their valence electron count only. Compounds with 24 valence electrons are semiconducting,

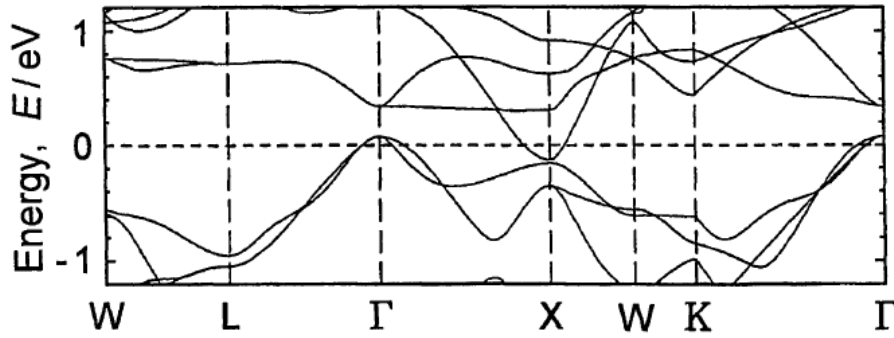


Figure 3.2. Band structure of Fe_2VAl showing a pseudogap at the Fermi level [23].

which is the case for Fe_2VAl , which is used as a starting material in this work.

Due to their flexible physical properties, Heusler compounds play a vital role in the search for thermoelectric materials. To improve the figure of merit, a high Seebeck coefficient, a low thermal conductivity and a high electrical conductivity are necessary. All of these features are shown or can be improved in Heusler compounds [7].

3.1 Fe_2VAl

This work focuses on the Heusler compound Fe_2VAl due to its interesting thermoelectric properties. Fe_2VAl exhibits semiconducting behavior over a wide temperature range. Figure 3.4 shows the band structure of Fe_2VAl near the Fermi energy. It has a pseudogap of about 0.1 eV to 0.2 eV at the Fermi level [20] and can therefore be seen as a semimetal. Large Seebeck coefficients have been observed for materials with high band masses, which is also true for Fe_2VAl with S exceeding $25 \mu\text{V K}^{-1}$ at room temperature depending on synthesis and heat treatment. The positive sign indicates electron holes being the primary charge carriers [7]. Its power factor can be improved to keep up with other thermoelectric material in use. However, a high thermal conductivity $\kappa \approx 28 \text{ W/m} \cdot \text{K}$ at room temperature prevents the figure of merit from reaching applicable levels [19].

Different approaches have been made to enhance the thermoelectric properties of Fe_2VAl by improving the power factor and/or reducing the thermal conductivity. One way to influence the electronic properties is to use offstoichiometric compounds. Fe_2VAl has 24 valence electrons per formula unit. This is expressed by the valence electron concentration (VEC), which is the number of valence electrons per atom. In case of stoichiometric Fe_2VAl , the VEC is 6. Mikami et al. fabricated $\text{Fe}_2\text{V}_{1-x}\text{Al}_{1+x}$ compounds with $-0.20 \leq x \leq 0.20$, thereby changing the VEC by changing the amount of valence electrons. Figure 3.3 shows the Seebeck coefficient as a function of the valence electron count. While S differs only slightly from 0 for stoichiometric Fe_2VAl , its

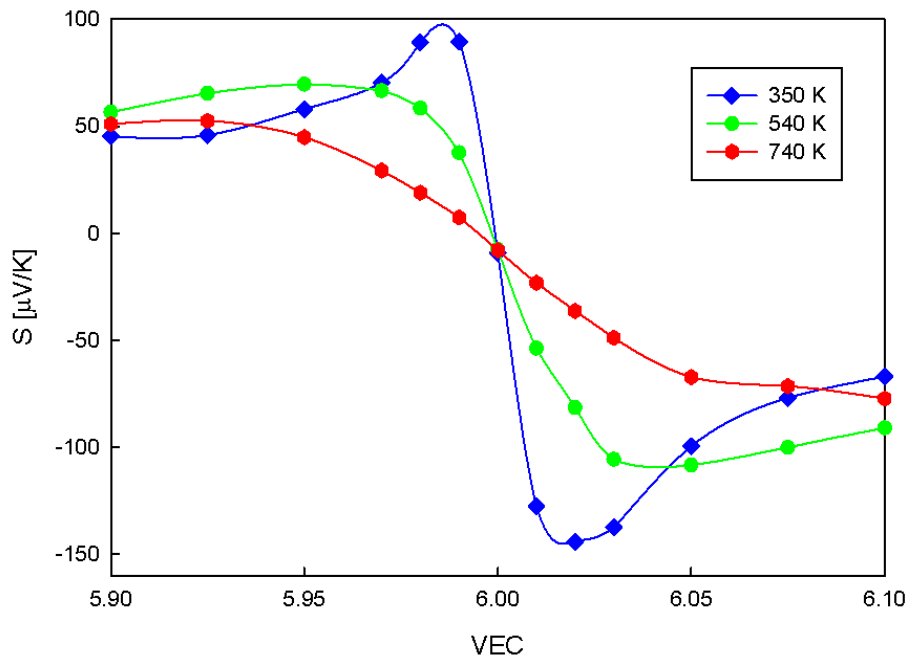


Figure 3.3. Seebeck coefficient of $\text{Fe}_2\text{V}_{1-x}\text{Al}_{1+x}$ as a function of the valence electron count, data from [20].

absolute value at room temperature rises sharply, when the VEC is changed slightly. At higher temperatures, the peaks are not as distinguished. In a rigid band model, changing the VEC raises or lowers the Fermi level without altering the electronic structure. By moving the Fermi level to a slope of the density of states on either side of the pseudogap, which can be seen in figure 3.2, the Seebeck coefficient rises according to Mott's formula, see equation 1.45. S is positive for a lower Fermi energy, which corresponds to an excess of electron holes and negative for a higher Fermi level and an excess of electrons. As another benefit, more charge carriers also reduce the electrical resistivity, which improves the power factor even further [20].

The thermal conductivity of any material consists of an electronic and a lattice part, as discussed in section 1.4. The Wiedemann-Franz law, equation 1.33, inseparably links the electronic part to the electrical conductivity. Improving the latter cannot be achieved without also enhancing the former. Therefore, efforts concentrate on the lattice contribution. One approach is to reduce the grain size of sample materials during production by sintering. This leads to a greater amount of grain boundaries and more phonon scattering and therefore, a smaller thermal conductivity [20].

By doping, the sample with heavy elements, the electrical and the thermal properties can be changed at the same time. The power factor is influenced by the introduction of more or less electrons, while the thermal conductivity is reduced by point defect

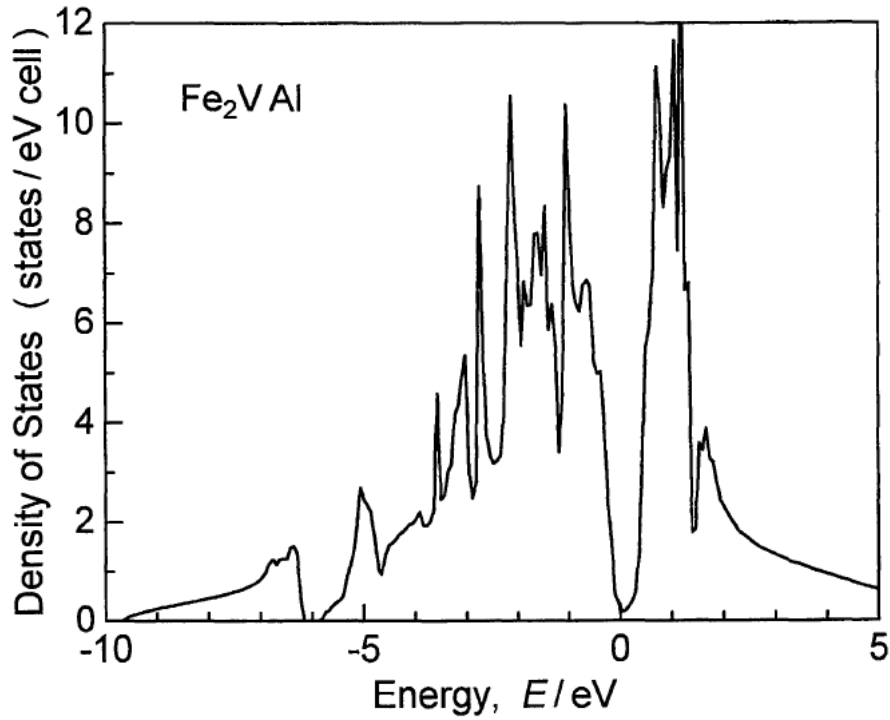


Figure 3.4. Density of states of Fe_2VAl as a function of energy [23].

phonon scattering on the lattice defects produced by the doped elements. Nonetheless, the impact of the doped elements on the electronic band structure has to be considered. Hinterleitner *et al.* report ZT values of about 0.22 in $\text{Fe}_2\text{V}_{1-x}\text{W}_x\text{Al}$ with $x = 0.1$ and a power factor of about $PF \approx 2 \text{ mW/m} \cdot \text{K}^2$. The thermal conductivity could be reduced to about 25% to $\kappa \approx 4 \text{ W/m} \cdot \text{K}$ for $x = 0.2$ [12].

Another recent approach of decreasing the thermal conductivity is to fabricate thin films by sputtering. These films consist of sub-micrometer sized grains, which again increase phonon scattering [21]. This method will be discussed in greater detail in this work.

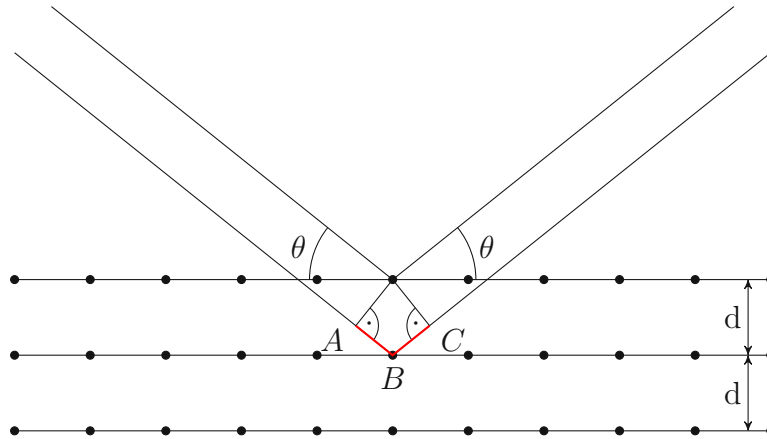


Figure 4.1. X-rays reflected on lattice plains. The path difference is given by $2d \sin \theta$.

4 X-ray Diffraction

X-Ray diffraction is a useful tool to investigate a sample's crystal structure. Generally, x-rays interact with matter by different mechanisms. For lower energies, the interaction of photons with atomic shells is predominant and they interact by coherent scattering (Rayleigh- or Thomson-Scattering), incoherent scattering (Compton-Effect) or by the photo effect. For higher energies, the photon's interaction with the atomic core becomes more important. In this energy range, the core photo effect or pair production is most common.

Using an x-ray source, photons can be directed onto a sample. Measurements of the scattered outgoing x-rays give insights on the properties of the sample. Depending on the used setup, different information can be gathered, including elemental composition, lattice parameters or lattice defects [5, 15].

X-rays which are scattered inside a crystal show distinct maxima for specific wavelengths at specific angles. According to Bragg, the radiation is reflected on different lattice plains and the reflected rays interfere with each other. Intensity maxima occur, if the path difference of two rays is a multiple of the wavelength, which is described by Bragg's law

$$n\lambda = 2d \sin \theta , \quad (4.1)$$

with n , λ , d , θ being the diffraction order, the wavelength, the distance between lattice plains and the reflection angle, respectively. Figure 4.1 shows a simplified model of an x-ray beam reflected on two lattice plains. The path difference \overline{AB} and \overline{BC} is given by $2d \sin \theta$. For a given wavelength, the location of the intensity maxima returns the distance between two lattice plains, which in turn gives information about the crystal structure [2].

In this work, the Bragg-Brentano setup "X'Pert Pro MPD" by PANalytical is used

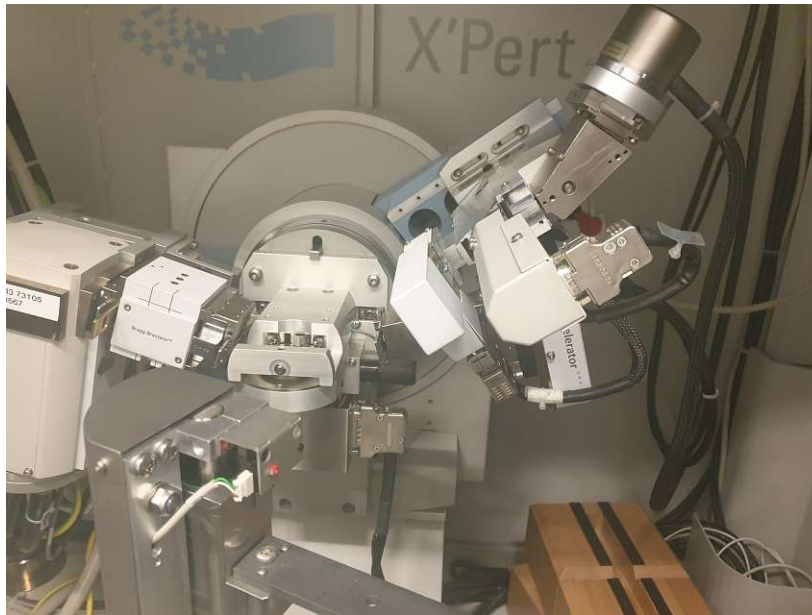


Figure 4.2. Bragg-Brentano diffractometer.

with the x-ray source on one end, the detector on the other end and the sample at the intersection, see figure 4.2. After grinding the sample to a fine powder in a mortar and spreading it on a glass plate, monochromatic Cu-K_α radiation is directed onto the sample, while the incidence angle is swept. The powder consists of many micro-crystals, which are randomly oriented. Therefore, for every incidence angle, there is a portion of crystals for which Bragg's law holds. By varying the angle θ , an intensity maximum is found, depending on d . Different lattice planes can be identified by peaks at different angles and give information about the presence or absence of certain phases.

This is used to make sure that the produced samples have the correct crystal structure. For doped and undoped Heusler compounds, disorder, as described in section 3, can be identified as well as possible phase changes after heat treatment.

4.1 X-ray Fluorescence

To examine the composition of a bulk sample, x-ray fluorescence can be used. This technique uses x-rays to induce emission of photons with a characteristic energy, which gives information about the concentration of the existing elements. The measured data are stored in PDF files, which are inconvenient for further analysis. Therefore, a Python script is designed, which extracts the data and returns it as a text file, as well as an excel file. The program can be found in appendix C.

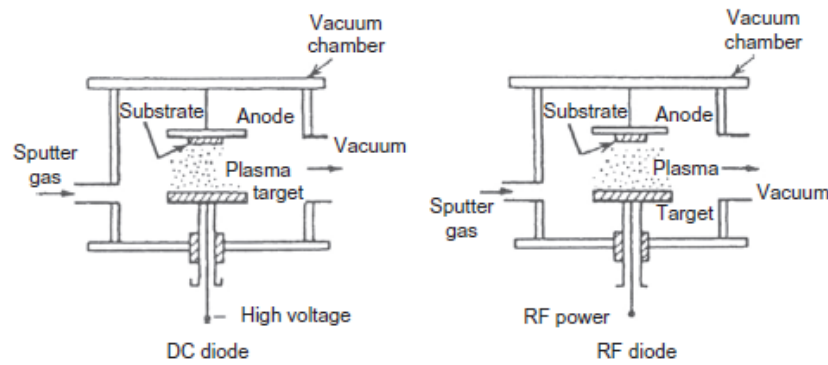


Figure 5.1. Setups for DC- and RF- sputtering [1].

5 Sputtering

There are several techniques to form a thin film of a desired material on a substrate including plating, chemical vapor deposition or evaporation. A widely used method is sputtering, which is used to create thin films with considerable growth rates. Sputtering is the process of bombarding a bulk target with ions. Thereby, material is ablated, which then condenses on a substrate to form a thin film.

5.1 DC-Sputtering

Direct current sputtering is the simplest sputtering setup. It consists of a target and a substrate, which are inside a vacuum chamber, as well as a power source, see figure 5.1. By applying a voltage between target and substrate within the vacuum chamber and inserting an inert gas at pressures in the Pa range, a glow discharge ignites. The gas is ionized and plasma forms. The positive ions are accelerated onto the target and hit the surface. Thereby, neutral particles are knocked out of the target, fly through the vacuum chamber and condense on the substrate. The plasma is sustained by secondary electrons being knocked out of the target by incoming ions, which are then accelerated to the anode and keep the plasma stable by collisions with the gas, as well as other electrons. The gas is usually argon, due to its inertness, favorable mass and low cost [18].

Though the setup is similar to the one of evaporation, sputtering has some advantages, which make it a very viable method. As the ejected particles have higher energies, their surface mobility is higher when depositing on the substrate. This leads to a more homogeneous growth and thus a more compact film. Furthermore, when sputtering an alloy, the composition of the surface changes, due to the different sputter yields of the constituents. As a result, there is an excess of the remaining elements, which then

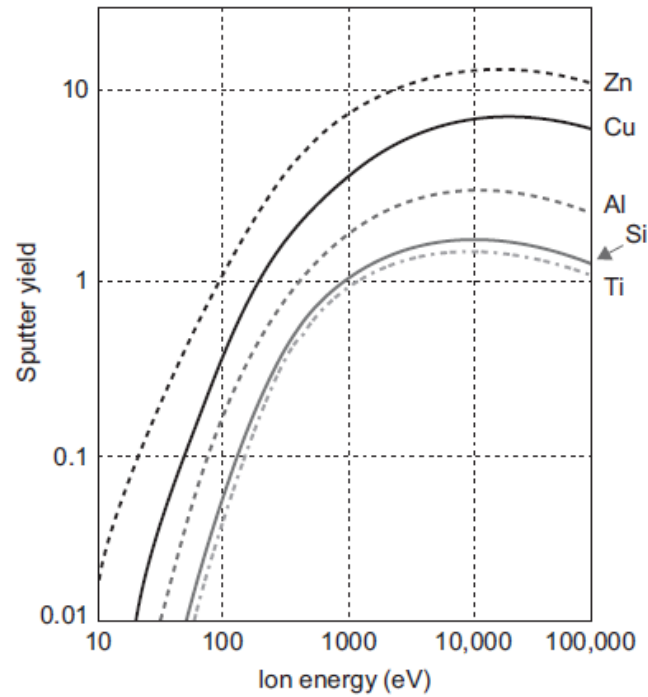


Figure 5.2. Sputter yield as a function of ion energy for different target materials [27].

have a higher probability to be sputtered. Thereby, after an equilibrium is reached, the stoichiometry of the film will be the same as the one of the target. Furthermore, the sputtering rates of the most commonly used metals are only within one order of magnitude, which further enhances stoichiometric coating [27].

The sputter yield Y is defined as

$$Y = \frac{\text{Number of ejected atoms}}{\text{Number of incident atoms}}. \quad (5.1)$$

A high yield leads to a higher coating rate, as more atoms leave the target and reach the substrate. The yield is dependent on the energy of the incoming atoms. For small energies, the binding energy of the target is too high and only loosely bound particles can be ejected. For energies around 10 eV - 1 keV the yield rises linearly as the incoming ions' velocity goes up. For very large energies, Y reaches a maximum as implantation of the ions leads to a reduction of the yield, see figure 5.2 [27].

While DC-sputtering, a part of the secondary electrons travels from cathode to anode without any scattering. These electrons are lost and don't contribute to the process. The ionization cross section has a maximum at ≈ 100 eV, so the ionization rate can't be improved by applying more power. This caps the maximum coating rate, which is why this method is not used industrially [27].

5.2 RF-Sputtering

The problem of DC-sputtering can be circumvented by using an alternating-current source, which is called RF-sputtering. Typically, a frequency of 13.56 MHz is used. The alternating forces keep the electrons longer inside the plasma, thereby enhancing electron densities, which in turn leads to higher ionization rates. Impedance matching hardware is used to tune the power supply to maximize the conveyed power [27].

An additional advantage of RF-sputtering is the possibility to sputter insulators. When using DC-sputtering with insulators, a voltage builds up on the surface of the target, which ceases the sputtering process. By replacing the direct current with a radio frequency power supply, this problem can be solved as any built up charge is freed by the changing polarity [1].

5.3 Magnetron Sputtering

Ionization can be further enhanced by magnetron sputtering. This is achieved by using RF-sputtering and adding a magnetic component behind or near the target. The magnetic field interacts with the electrons inside the plasma via the Lorentz force and bends their trajectory to form spirals. This further elongates their path inside the plasma and leads to a higher ionization probability and thereby to a higher sputtering rate. Usually, the magnetic field lines are parallel to the target surface and perpendicular to the electric field, which leads to cycloidal electron paths above the target. For stationary magnet positions, the target will not be homogeneously ablated, as the field lines are not evenly spaced, as can be seen in figure 5.3. Therefore, the magnets are often mounted on rotating racks to even out possible inhomogeneities [27].

5.4 Sputter Etching

Sputter etching is the process of removing material from a sample and is therefore the reversed process of normal sputtering. Substrate and target switch places, which can be achieved by changing the polarity of the electrodes. Sputter etching is used to clean the surfaces of samples from contamination or oxides but can also be used to ablate any unwanted material.



Figure 5.3. Used sputter target with ablation ring.

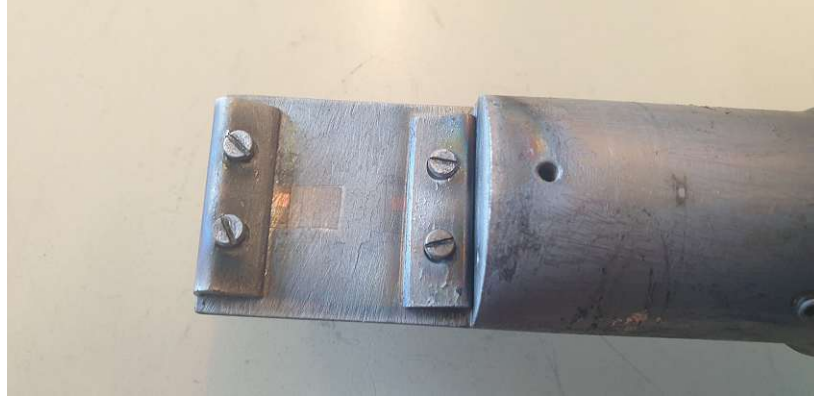


Figure 5.4. Substrate holder.

5.5 Intensity Distribution

For thin films, the film thickness is an essential parameter, influencing many different properties. Usually, it is supposed to be homogeneous over the whole sample. Thickness measurements are therefore very important when thin films are sputtered. In this work, magnetron sputtering is used to produce thin films on a planar substrate, which is mounted on a substrate holder, as seen in figure 5.4. To get homogeneous films, the intensity distribution of the incoming particle flux has to be considered.

The amount of particles, condensing on the substrate, highly depends on the target-substrate geometry. In the simplest model, a small spherical source evaporates particles from its area A_e with a constant rate Γ_e , see figure 5.5. The total sputtered mass is given by

$$m_e = \int_0^t \int_{A_e} \Gamma_e dA_e dt' . \quad (5.2)$$

The amount of mass reaching the substrate depends on the distance r and the inclination angle α of the substrate. The projection of the substrate's area A_S on the area of a sphere with radius r is given by $A_S \cos \alpha$, which holds if A_S is sufficiently small. The source sends out particles uniformly in every direction. Therefore, the amount of mass reaching the substrate is proportional to the ratio of the substrate's area to the total area of the sphere.

$$\frac{dm_S}{dA_S} = \frac{m_e \cos \alpha}{4\pi r^2} \quad (5.3)$$

Usually, the sources are not point-like but rather surface sources. The emitted particles are distributed only over a half sphere with a $\cos \theta$ -dependence. The incoming mass per unit area is given by

$$\frac{dm_S}{dA_S} = \frac{m_e \cos \theta \cos \alpha}{\pi r^2} . \quad (5.4)$$

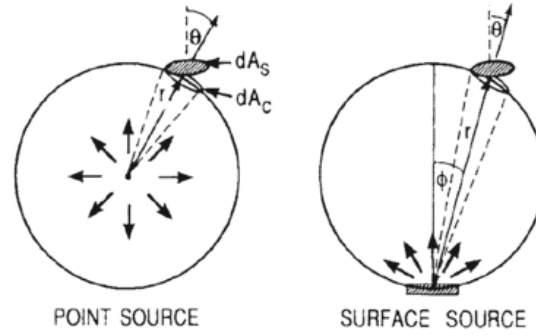


Figure 5.5. Angular distribution of a point source and a surface source, [24].

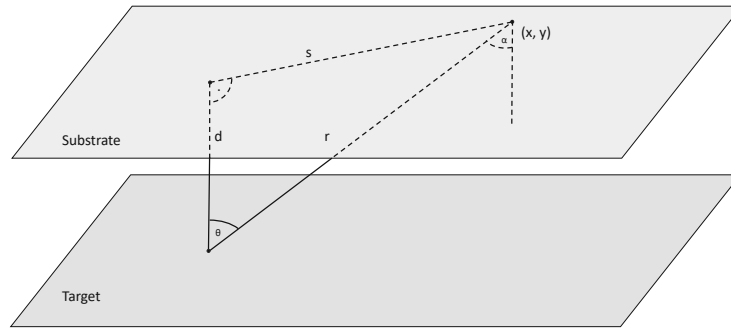


Figure 5.6. Parallel target-substrate geometry.

From empiric data one can find a $\cos^n \theta$ dependence of the angular distribution. Higher values of n are related to a more directed particle flux. Assuming a $\cos \theta$ dependence, a uniform film thickness can be achieved by placing the source and the substrate tangential to the surface of a sphere. This leads to an angular independent film thickness [24].

For planar sources and substrates, which are parallel to each other, $\theta = \alpha$ holds. Using $\cos \theta = d/r$, with d being the distance between source and substrate, equation 5.4 becomes

$$\frac{dm_S}{dA_S} = \frac{m_e \cos^4 \theta}{\pi d^2}. \quad (5.5)$$

This geometry is used in this work and can be seen in figure 5.6. Magnetron sputtering ejects particles from the target, where the magnetic field lines generate the highest electron densities. With circularly arranged magnets, this leads to a ring-shaped ablation. An expression proportional to the distribution of particles sent out from an infinitesimal area within the ring, identified by the angle ϕ_t , is given by $G(\phi_t, x, y)$ in

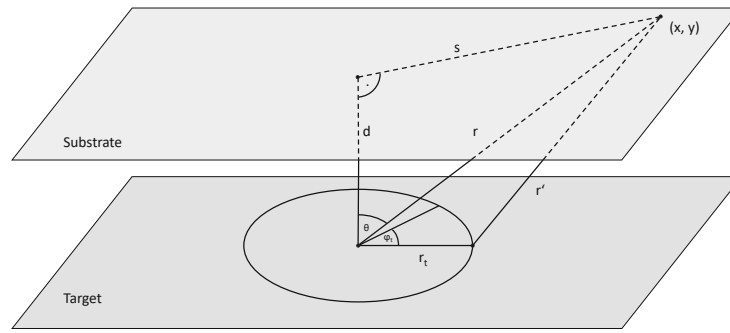


Figure 5.7. Ring-shaped target with parallel planar substrate.

equation 5.6. A sketch of the used geometry is given in figure 5.7.

$$G(\phi_t, x, y) = \frac{d^4}{[d^2 + (x - x_t - r_t \cos \phi_t)^2 + (y - y_t - r_t \sin \phi_t)^2]^2} \quad (5.6)$$

x and y are Cartesian coordinates in the substrate plane, r_t is the radius of the ring. The origin is located above the center of the ring. x_t and y_t are constants, representing a possible shift of the target with respect to the origin.

To find the contribution of the total ring, equation 5.6 is integrated over the whole ring. This is done numerically using *Mathematica* [29]. The result is normed by the value of the integral at the center of the target.

$$I(x, y) = \frac{\int_0^{2\pi} G(\phi_t, x, y) d\phi}{\int_0^{2\pi} G(\phi_t, x_t, y_t) d\phi} \quad (5.7)$$

The percentage of particles reaching the target with respect to all emitted particles is calculated by integrating over the substrate's area and dividing by the integral over the whole space.

The *Mathematica* script which returns the discussed functions is given in appendix B.

The calculated intensity gives the same results as the calculation in [24], but returns values for Cartesian coordinates and for off-center sputter rings.

Figure 5.8 shows plots of $I(x, y)$ with $y = 0$ for a ring with $r = 7$ mm at substrate-target distances from 5 to 70 mm. The substrate holder is about 25 mm wide. For small values of d , the influence of the ring is clearly visible, with maxima above the ring and steep slopes. For large distances this influence decreases and the distribution becomes nearly constant. This homogeneity comes at the cost of longer sputtering times as a lot

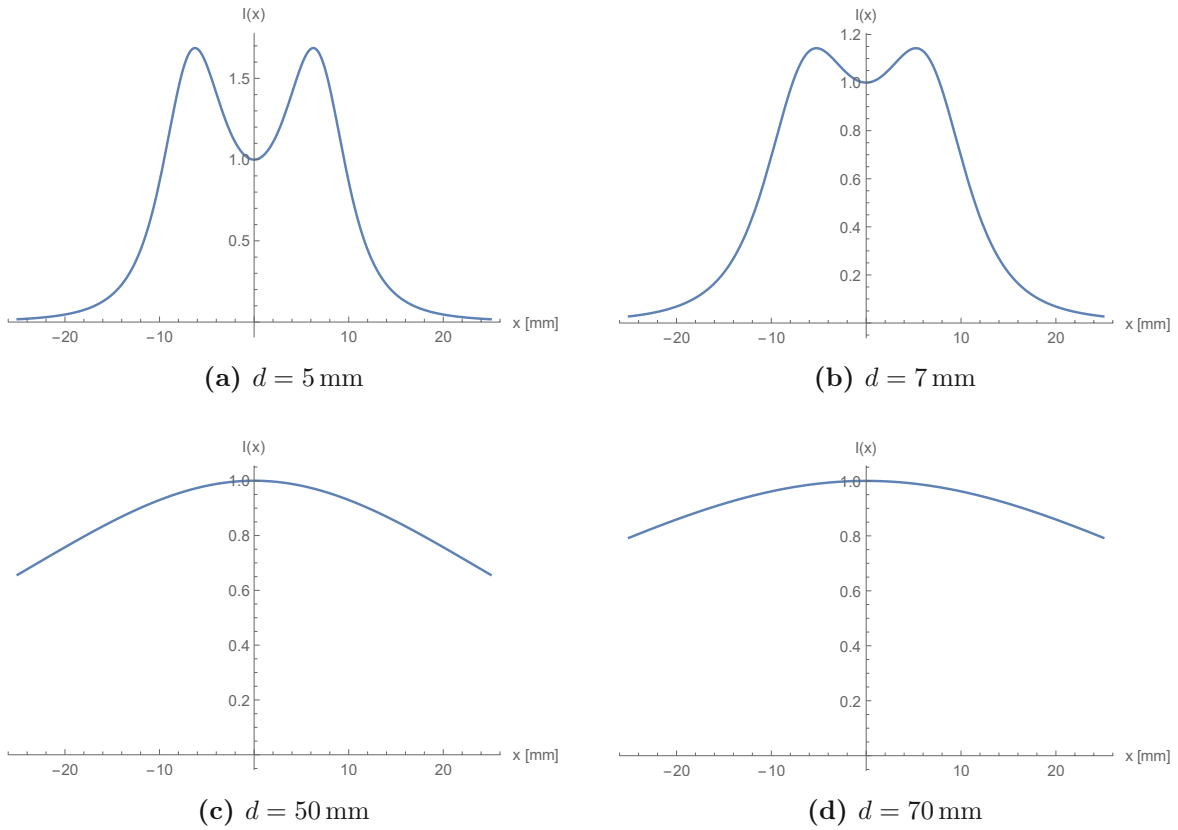


Figure 5.8. Intensity distribution $I(x, y)$ with $y = 0$ for a sputtering ring with $r = 7$ mm at different substrate-target distances.

of flux is lost to the surroundings. While the amount of particles reaching the substrate holder is 76% of the total ejected particles for $d = 5$ mm and 65% for $d = 7$ mm, it goes down to 6% and 3% for $d = 50$ mm and $d = 70$ mm, respectively. For small samples an optimum can be found, where the variance of the intensity in the middle is low and the particle flux is still high, see figure 5.8b. In this work, however, longer sputtering times were accepted with the advantage of a certain homogeneity over the whole substrate holder. The percentages are calculated using the script in appendix B by integrating $I(x, y)$ over the dimensions of the sample holder and dividing by the integral over the whole plane. The sample holder's length and width are set as 25 mm and 2 mm, respectively. In appendix B, there are plots of the intensity for a target shifted in x-direction for $x = 0$ and for $y = 0$, as well as a 3D plot of the intensity.

6 Material Synthesis

When sputtering thin films on a substrate, a target has to be manufactured first. To produce bulk slabs and targets with the right stoichiometry, pure elements are weighed in. Samples with a mass of 35 g are usually big enough for two targets. In this work only metals are used, which can be sawed into small pieces using a common handsaw. Each element is cut into several parts to ensure a more even distribution when melting. Sharp edges, which result from sawing, are filed to prevent fragments from chipping off, which would distort the results. By carefully removing material, the mass can be determined up to 10^{-4} g using a high precision scale.

The initial elements are put in a water cooled Hukin crucible for induction melting, which is powered by a 30 kW generator using a frequency of about 600 kHz [14]. The synthesis is performed inside a quartz tube, which is evacuated to remove oxygen and filled with argon to prevent the samples from evaporating. Figure 6.1 shows the crucible with the cut and filed samples inside, before as well as during melting.

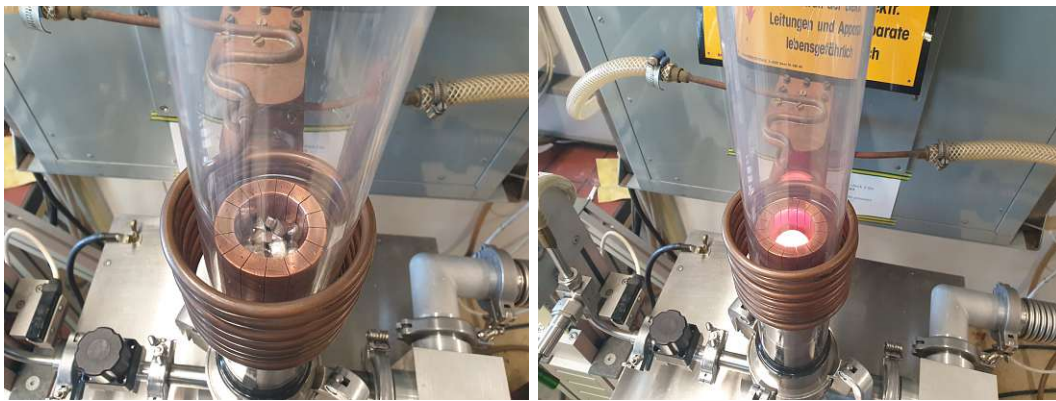


Figure 6.1. *left:* Hukin crucible with cut samples inside; *right:* Hukin crucible during melting.

The sample is melted down three times and turned over after each step, to get a more even mix. A small portion of the sample evaporates nonetheless during the melting process, which can alter the final composition. To ensure this error is small, the sample is weighed after every step, which allows an estimation of the stoichiometric deviation. The difference in mass before and after three melting processes is consistently below 0.1 %. During the last melting, the power is reduced very slowly to minimize internal stress, which could lead to cracks in the sample. If there are visible cracks, the sample has to be melted again, as the target can break when being cut.

After synthesis, the sample is cut into pieces using an aluminium oxide cutting disc. A 35 g sample can be cut into two targets with a diameter of about 25 mm and a height of three millimeters, as well as several cuboids with the dimensions 10 mm \times 2 mm \times 2 mm. The remaining fragments can be ground into a powder for x-ray diffraction.

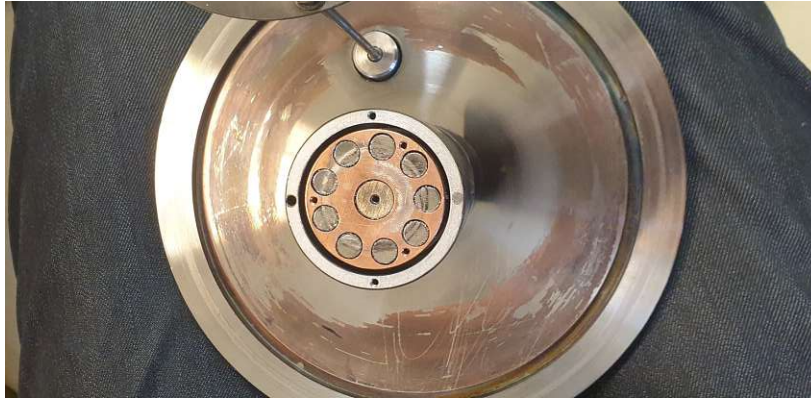


Figure 6.2. Target holder without target. Inside the grounded shielding one can see the copper cylinder with circularly arranged magnets.

6.1 Thin Film Production

To produce thin films, a DC magnetron sputtering system, as mentioned in section 5, is used. It consists of a vacuum chamber into which the target holder and the substrate holder can be inserted. The chamber is evacuated down to 10^{-4} Pa by a turbomolecular pump and a preceding rotary pump. To change the substrate without opening the chamber, a vacuum lock is mounted on one side, which can be evacuated by a separate rotary pump. The chamber can be filled with argon, which is used as sputtering gas.

The target holder is connected to the power supply and is put inside the vacuum chamber. It consists of a copper cylinder, into which magnets can be inserted, which create the magnetic field required for magnetron sputtering, as can be seen in figure 6.2. The target is placed on top of that with a thin copper grate in-between, to improve electrical contact. The target is held in place by a ring, which is mounted on the outer edge of the target, to leave a lot of surface area free for sputtering. Isolated from this part, a shielding encases the target holder, which ends in a cap set right above the target. With the target on negative potential and the shielding being grounded, the applied voltage leads to the sputtering plasma. The cap has a hole, matching the free surface area on the target, through which the sputtered particles fly to the substrate. Figure 6.3 shows the target holder with the target built in. One can see the grounded shielding on top, the ring holding the target is hidden beneath it. On the target, a ring of lighter color marks where the magnetic field leads to higher ablation. Figure 6.4 shows the target holder inside of the vacuum chamber. The substrate holder is not inside and would be aligned with the target.

The substrate holder is a hollow cylinder mounted on a metal rod which can be pushed through the vacuum lock into the chamber, as shown in figure 6.5. The cylinder is isolated from the rod but connected to an outside plug to be grounded. On the inside, there is a heating cartridge, which is used to keep the substrate at a certain

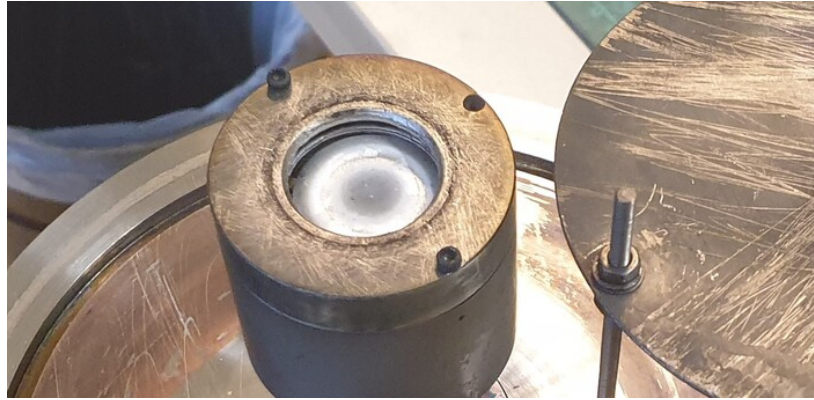


Figure 6.3. Target holder with target built in.



Figure 6.4. Inside of the vacuum chamber with built-in target holder.

temperature. The substrate itself can be mounted on the flattened side in one of two slots and is held in place by clamps. As discussed in section 5.5, the distribution of the sputtered particles has to be considered. To use both substrate positions for the same measurement series, the distance between target and substrate has to be large for a uniform coating rate. Even so, it is preferable to use only one position for one measurement series. The whole system can be rotated and must be aligned with the target holder. As mentioned, the distance between target and substrate can be manipulated by retracting the target holder.

Prior to this work, the sputtering process has been started with the substrate facing the side opposite of the target. This way, possible contamination or an oxide layer can be removed from the target before coating starts. After this transient phase the substrate holder is turned 180° to face the target, which starts the coating process. This method requires the operator to turn the substrate holder quickly as well as precisely, which hinders repeatability. Therefore, a shutter is designed, which separates substrate and target. It consists of a steel plate connected to a rod, which leads through a vacuum cover to an outside mechanism, as can be seen in figure 6.6. This allows the shutter to be put in front of the target, thereby shielding the substrate from incoming particles.



Figure 6.5. Inside of the vacuum chamber with built-in substrate holder.



Figure 6.6. Vacuum cover with shutter mechanism.

To start and stop coating, the shutter is opened or closed independent of the starting phase. To implement the shutter, the vacuum lid has been modified by drilling a hole through it, which fits the shutter's o-ring. Two threaded holes, about half of the cover's thickness deep, are included to be able to fixate the shutter on the cover by two screws, see figure 6.7. The built-in shutter in open position can be seen in figure 6.8.

During sputtering the substrate is grounded, while the power supply is set to about 15 W, which leads to a voltage of about 300 V and a current of about 0.05 A. With these settings an argon pressure of 2 Pa is used.

To control the coating rate, a test sample is produced and the film thickness is measured using a profilometer, as seen in figure 6.9. When the substrate – made of glass for the test sample – is clamped down, the covered area is not coated, which forms an edge. The profilometer pulls a stylus across the sample's surface, which eventually falls down the edge. The height of this drop is equal to the film's thickness. The coating rate can be calculated from the film thickness and the sputtering time. To prevent measuring errors, the film thickness is measured about five times at different places along the edge to calculate a mean thickness. Only polished substrates like silicon or



Figure 6.7. Vacuum cover modified for the use of target holder and shutter.



Figure 6.8. Target holder with shutter in open position.

glas wafers are suitable because flat surfaces are needed as reference. The profilometer measures the displacement of the stylus at the end of the measuring arm with respect to its reference point. The reference is a red ring, as seen in figure 6.9, which slides across the substrate. It is important to start measuring with the stylus on the film and the ring on the substrate. If the ring starts on the film, it will fall down the edge, which will result in a discontinuity in the measured data. Also, the measured edge has to be far away from the end of the substrate. Otherwise, the ring will slide off the substrate, which leads to a steep increase of the measured thickness. Figure 6.10 shows the measurement data from which the film height is calculated.

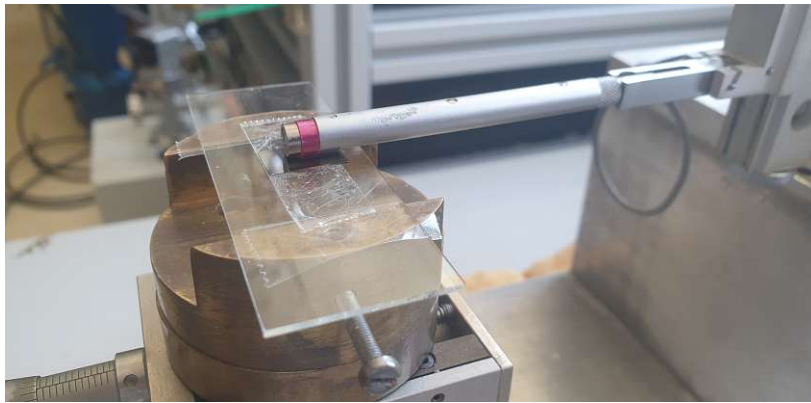


Figure 6.9. Using a profilometer to measure the film thickness of a sample.

The substrate temperature has great influence on the film's properties. Therefore, the temperature is controlled by the heating cartridge inside the substrate holder. It can heat the sample up to 500 °C, although using high coating temperatures greatly elongates production time, because the sample has to heat up and cool down before moving to the next substrate. To prevent oxidation, the sample should not be taken out of the chamber as long as it hasn't sufficiently cooled down, depending on how reactive the used material is.

After sputtering, the films are usually heat treated. This is done by sealing the samples

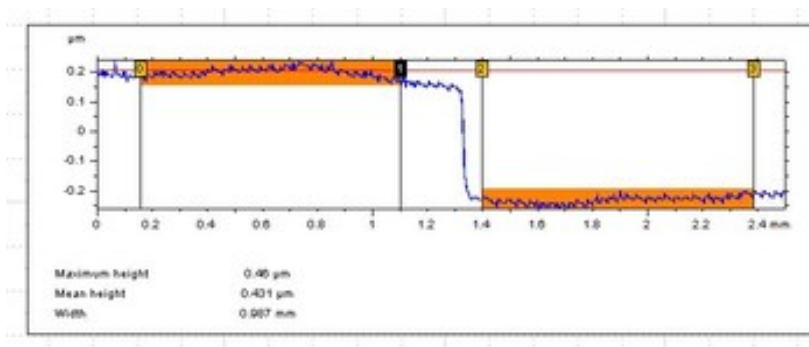


Figure 6.10. Profile measurement.

in evacuated quartz pipes, which are then put into an oven. In most cases, the films are heated to 450 °C for seven days.

6.2 Etching

Sputtering can not only be used to produce thin films but also to remove unwanted material from the target. This sputter etching was discussed in section 5.4. In this work, the sputtering chamber was repurposed, being able to sputter and etch alternately.

To use the chamber in etching mode, another component, the magnet holder, has to be inserted. When using the sputtering chamber to etch a sample, the substrate holder is set to a negative potential and acts as the new target. The magnet holder consists of a grounded steel plate, acting as the second electrode, and a magnetic system, which allows magnetron sputtering. Figure 6.11 shows the setup of magnets which induce the magnetic field. The magnet holder, fixed on a retractable rod, can be seen in figure 6.12. This part and the substrate holder are aligned and brought to a separation of about 4 cm. The exact distance is determined by slowly changing it, while measuring the sputtering current. When the current reaches a maximum for a given pressure, the system is fixed in place. Note that the magnetic system is movable, so it can be pulled back to the top of the chamber, where it is not influencing the substrate holder anymore. Figure 6.13 shows a simplified model of the vacuum chamber. The magnet holder is in the lower position, which is used for etching and it and the substrate holder are facing each other.

On the bottom of the chamber the target holder is located, with the movable shutter above, which was discussed in section 6.1. By turning the substrate holder, retracting the magnet holder and opening the shutter, a sample can be alternately sputtered and etched without venting the chamber.

For etching, a power of 15 W is used, which is the same as for sputtering but the pressure has to be slightly increased to 8 Pa.

As the substrate holder acts as the new target, its geometry plays an important role for the layout of the electrical field lines, which in turn influence the etching process. Therefore, the initial substrate holder is exchanged for one with a more suitable geometry as can be seen in figure 6.14.

A DC source powers the process, so only conducting samples can be etched. The surface of insulators would be charged instantly by the incoming ions, which would stop the etching process. For conducting films on insulating substrates, the film has to be connected to the negative potential. This was first achieved by fixing the sample



Figure 6.11. Magnet holder.



Figure 6.12. Magnetic setup used for sputter etching.

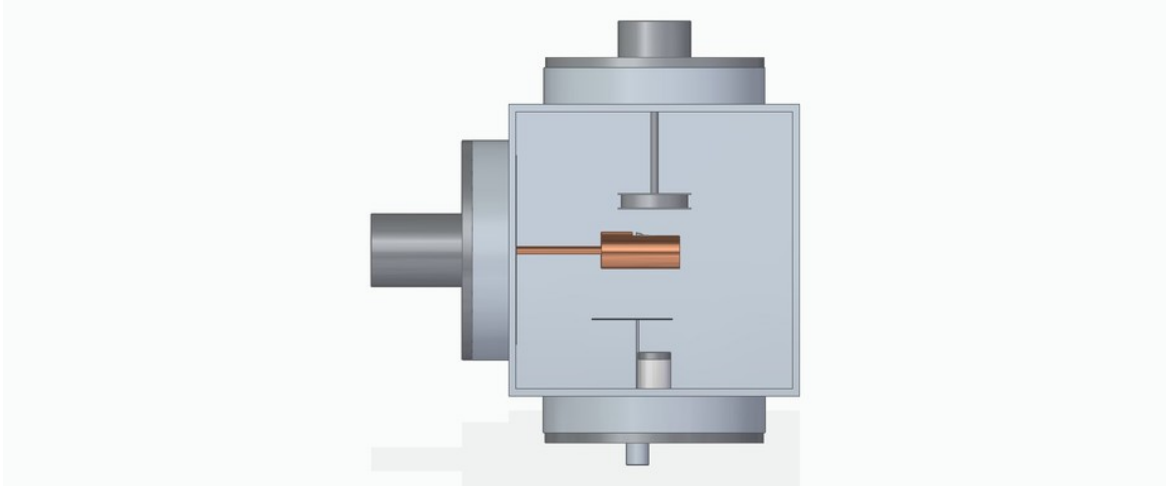


Figure 6.13. Model of the vacuum chamber with the etching setup: magnet holder (top), substrate holder (mid) and target holder (bottom).

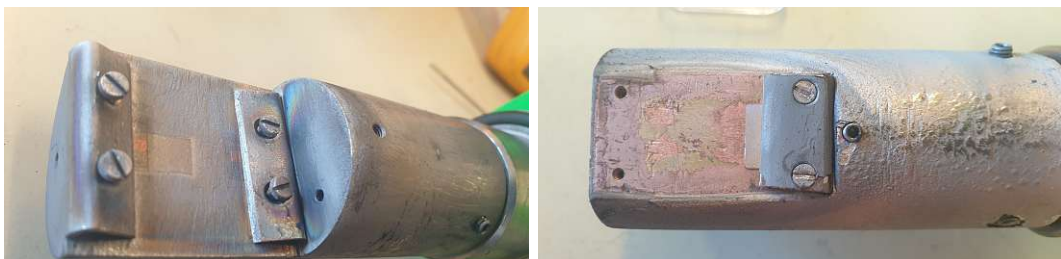


Figure 6.14. *left:* Substrate holder with a sharp edge above the sample; *right:* Nearly planar substrate holder.

with the clamps on the substrate holder, as seen in figure 6.14. Although this brought the film to the necessary potential, the substrate holder and the clamps are on the same potential and are etched as well. Since the clamps rise up above the sample, they will be etched more than the film and will contaminate the sample. Therefore, a new part is introduced. A glass plate, with a small copper band wrapped around it, is put between clamp and sample, as seen in figure 6.15. The copper band is maintaining electrical contact by pressing the tip on the film, while minimizing the contamination through its small surface. The glass plate shields the sample from contamination through the clamp and increases the distance between them.



Figure 6.15. *left:* Clamp with glass plate to increase the distance to the sample, a copper band maintains the electrical contact; *right:* side view.

Figure 6.16 shows a model of this setup inside the vacuum chamber as well as the substrate holder with an etched sample.

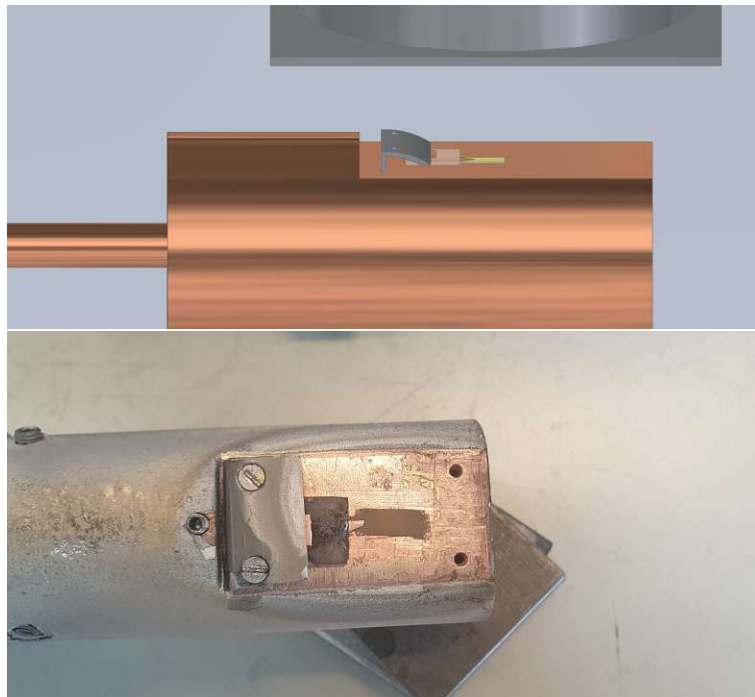


Figure 6.16. *top:* Model of the setup with a sample prepared for etching; *bottom:* a sample after etching.

This setup is used to etch thin films, which were formerly produced by sputtering. Figure 6.17 shows a film that took on a darker color during heat treatment, probably

due to oxidation. After etching, the color change is reverted to its original tone. This is a first indicator, that the film was properly etched and the even color switch suggests an as even etching distribution.



Figure 6.17. Comparison of a sample before (*top*) and after (*bottom*) etching.

Determining the etching rate turns out not to be an easy task. An approach to measure the thickness directly with a profilometer, as discussed in section 6.1, is not possible with the used setup, as there are no edges to measure. Putting a mask on top of parts of the sample to create this edge did not produce definitive results, possibly due to charge building up on the mask, which influences the electric field lines.

An alternative approach is to measure the mass of the sample before and after etching with a high precision scale but the removed material is not enough to lead to usable results.

In this work the etching rate is determined indirectly by measuring the electrical resistance of a thin film. If the thickness d decreases, the resistance increases according to equation (6.1).

$$R_{film} = \frac{\rho l}{bd} \quad (6.1)$$

with the resistivity ρ , the film width b and the film length l . Note that this assumes homogeneous etching and a negligible conductivity contribution by the substrate.

Figure 6.18 shows an SEM image of a Fe_2VAl film on an unpolished silicon substrate at a magnification of 5000x. For comparison, figure 6.19 shows a $\text{Fe}_2\text{V}_{0.8}\text{W}_{0.2}\text{Al}$ film that was etched. One can see the geometric shapes of the silicon wafer in both images. The etched film is a lot less smooth than the other film.

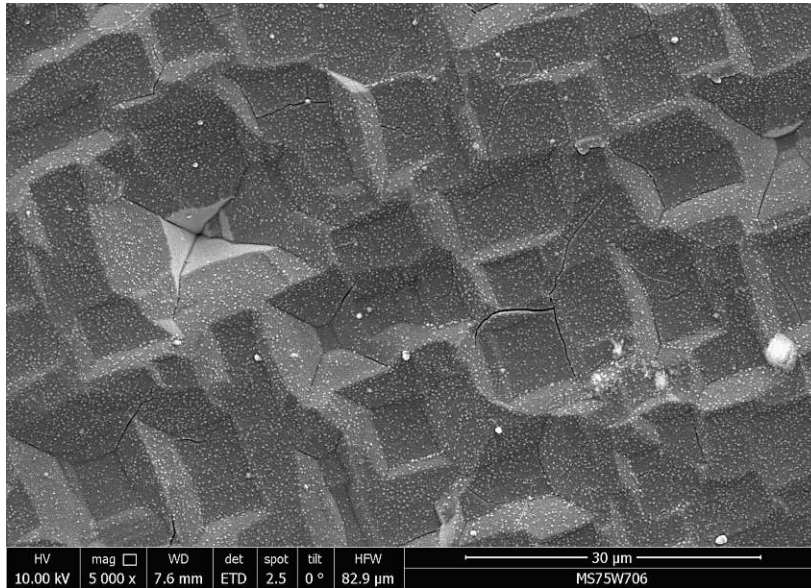


Figure 6.18. SEM picture of a Fe_2VAI film with a thickness of $0.5\ \mu\text{m}$ on an unpolished silicon substrate.

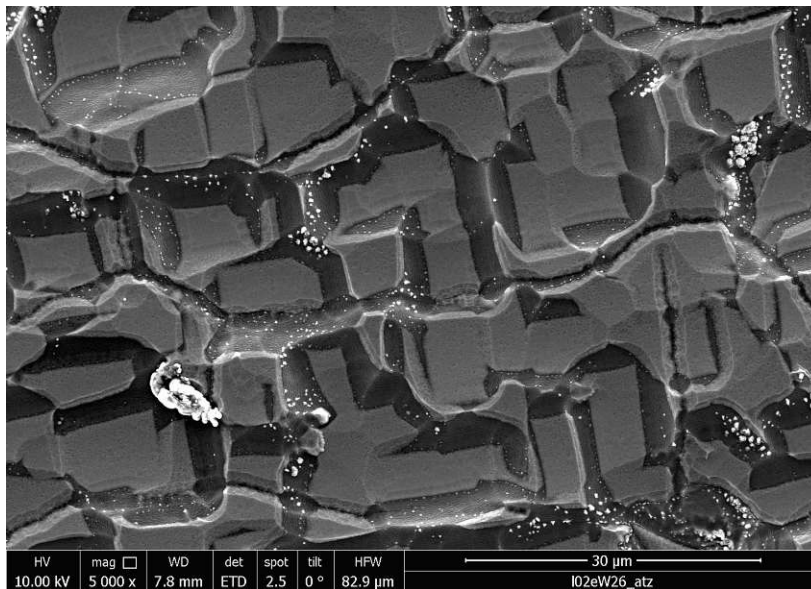


Figure 6.19. SEM image of a $\text{Fe}_2\text{V}_{0.8}\text{W}_{0.2}\text{Al}$ film after etching.

7 Thin Films

A thin film is a layer of a material condensed on a substrate. Its thickness is orders of magnitude smaller than its other dimensions. Thin films have a lot of different applications in many technological fields such as electronics, optics or tribology due to their versatility. Their physical properties can differ significantly from bulk materials due to the film's growth process as well as size effects, which makes thin films interesting on their own, as well as in combination with a suitable bulk material [1].

7.1 Substrate-Film System

7.1.1 Electrical Resistivity

The electrical resistivity of thin films is an important property, not only in thermoelectrics. It is measured by determining the resistance of a sample with known geometric parameters. The relationship between resistance R and resistivity ρ for a homogeneous sample with length l , width w and height h is

$$\rho = \frac{Rwh}{l}. \quad (7.1)$$

Measurements of the resistance are performed by applying a voltage to a sample while measuring the current or vice-versa, according to Ohm's law

$$R = \frac{U}{I}. \quad (7.2)$$

This can be done by connecting copper wires at the ends of the sample. This two-point technique is good for approximate measurements but can incite errors. The resistance of the wires, of the contacts with the sample and the inner resistance of the measurement devices alter the results.

A more proper technique for samples in the shape of a rectangular bar is the four-point method. Four wires are attached to the sample as can be seen in figure 7.1. A constant current is applied to the outer wires, while the voltage drop is measured at the two inner contacts. This method ignores wire and contact resistances and gives more accurate results. The four-point technique is also suitable for thin films, as long as a rectangular shape with a constant thickness and homogeneity can be assumed. For thin films, the contacts are usually pressed onto the surface of the probe.

For samples of arbitrary dimensions the four-point method is not suitable anymore. These measurements can be done using the van der Pauw method [10].

Usually, the substrate has a resistivity orders of magnitude larger than the film. In

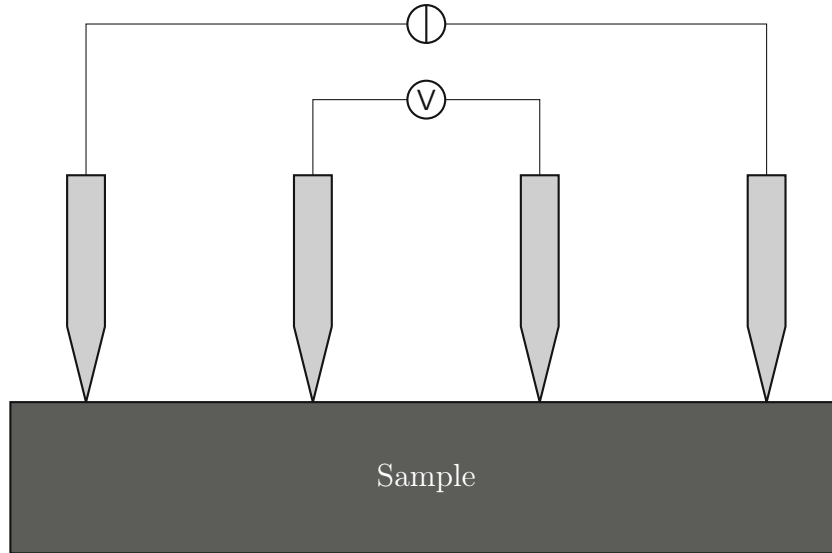


Figure 7.1. Four-point measurement configuration.

this case the current running through the substrate can be neglected and the measured resistance is equal to the film's. If not, the substrate-film system has to be considered as a whole. It can often be imagined as two rectangular bars put together with the same length and width but different heights. The measured R_M is the resistance of two parallel conductors, given by

$$R_M = \frac{R_F R_S}{R_F + R_S} . \quad (7.3)$$

R_F and R_S are the resistances of the film and the substrate, respectively. Inserting equation 7.1 and using the geometric relations $l_F = l_S = l$ and $w_F = w_S = w$, this can be written as

$$R_M = \frac{\rho_F \rho_S \frac{l}{w}}{\rho_F h_S + \rho_S h_F} \quad (7.4)$$

If the influence of the substrate is wrongfully neglected, the measured resistance is believed to come from the film only, hence the measured resistivity ρ_M is calculated with the film's dimensions.

$$\rho_M = \frac{\rho_F}{1 + \frac{\rho_F h_S}{\rho_S h_F}} \quad (7.5)$$

The error made by neglecting the substrate's influence is depending on the factor $\frac{\rho_F h_S}{\rho_S h_F}$ and becomes relevant for high film resistivities or small film thicknesses with respect to the substrate.

7.1.2 Seebeck Coefficient

A temperature difference induces a Seebeck voltage in a thermoelectric material. To measure the Seebeck coefficient of the film and the substrate, both are connected to

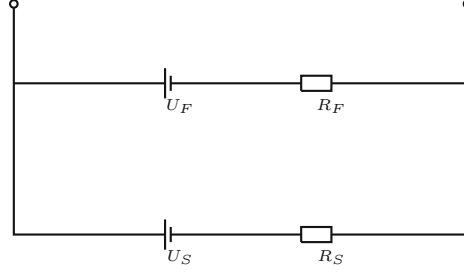


Figure 7.2. Equivalent circuit diagram of a substrate-film system.

temperature baths and have to be considered as a substrate-film system. This can be represented by the circuit in figure 7.2. Substrate and film are depicted as two parallel, real voltage supplies with the voltages U_S and U_F and the inner resistances R_S and R_F , respectively. To get the total voltage U_{tot} , one source is shorted and the current from the remaining source is calculated. Then, the current is calculated again after shorting the other source. The total current is the superposition of the two currents. With that, Kirchhoff's rules can be applied and the total voltage can easily be shown to be

$$U_{tot} = \frac{U_S R_F + U_F R_S}{R_F + R_S} . \quad (7.6)$$

The film usually covers the whole area of one side of the substrate, therefore the length and the width of substrate and film are equal

$$l_F = l_S = l \quad (7.7)$$

$$w_F = w_S = w . \quad (7.8)$$

Inserting equations 7.7 and 7.8 into 7.6 leads to

$$U_{tot} = \frac{U_S \frac{\rho_F l}{wh_F} + U_F \frac{\rho_S l}{wh_S}}{\frac{\rho_F l}{wh_F} + \frac{\rho_S l}{wh_S}} \quad (7.9)$$

$$= \frac{U_S \rho_F h_S + U_F \rho_S h_F}{\rho_F h_S + \rho_S h_F} . \quad (7.10)$$

The voltage produced by the Seebeck effect from a temperature difference ΔT is

$$U = S \Delta T , \quad (7.11)$$

with the Seebeck coefficient S . With that, the Seebeck coefficient of the combined substrate-film system can be written as

$$S_{tot} = \frac{S_S \rho_F h_S + S_F \rho_S h_F}{\rho_F h_S + \rho_S h_F} \quad (7.12)$$

or alternately using the conductivities σ ,

$$S_{tot} = \frac{S_S \sigma_S h_S + S_F \sigma_F h_F}{\sigma_S h_S + \sigma_F h_F}. \quad (7.13)$$

This result can be generalized to an arbitrary number i of parallel thermoelectric parts with the same width and length

$$S_{tot} = \frac{\sum_i S_i \sigma_i h_i}{\sum_i \sigma_i h_i} \quad (7.14)$$

which is a result also given in [13]. Equation 7.13 gives important information about the substrate's influence and whether it can be neglected. When measuring the Seebeck coefficient of the film, the product of the substrate's Seebeck coefficient and electrical conductance has to be orders of magnitude smaller than the product of the film's parameters, for the substrate to be negligible. If there is an interface layer between substrate and film which has distinct features, this system can be described by equation 7.14.

8 Measurements

Resistivity and Seebeck measurements of bulk and thin film samples are performed using an *ULVAC ZEM-3* [28] unit. Measurements are performed under low-pressure helium atmosphere inside a furnace, which controls the surrounding temperature in a range from room temperature to about 800 K. The electrical resistance is measured using the four-point method. After each measurement, the polarity of the applied current is changed and the resistance is measured again. With known dimensions, the resistivity is calculated subsequently. Figure 8.2 shows a bulk sample being held by the outer electrodes and two contacts coming from one side. The Seebeck coefficient can be measured simultaneously by heating the contact on the bottom. The resulting temperature gradient in the sample is measured by the middle contacts, which are two thermocouples. The temperature gradient generates a Seebeck voltage which is also measured by the inner contacts. Separate measurements with three temperature differences are performed for each step.

To measure thin films, the sample is mounted on an insulator, which holds the sample in place by platinum plates and connects the film to the outer electrodes. To minimize contact resistance, graphite strips are put between film and connectors, see figure 8.2.

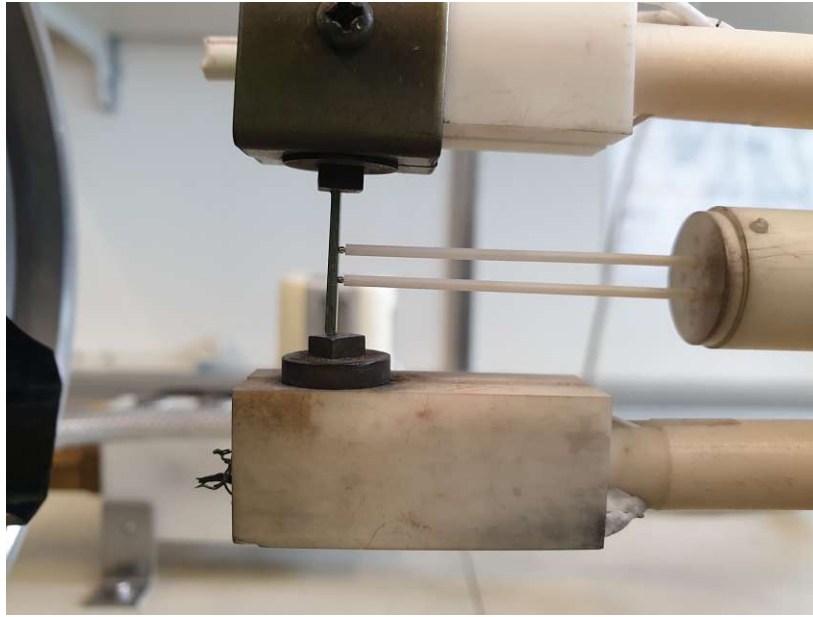


Figure 8.1. Four-point measurement of a bulk sample for measuring resistivity and Seebeck coefficient.



Figure 8.2. Four-point measurement of a thin film. The film is mounted on an insulator. Graphite strips between film and connectors cater for good electrical contact.

The data measured by the *ULVAC* device is stored in a text file. Using a program, this file can be analyzed to process the raw data. During this routine, mean values from four measurements and the power factor are calculated and process specific data like time steps and error codes are omitted. To further improve usability, a separate *Python* script is designed, which is shown in appendix A. It transforms the already analyzed file in a way which can be imported more easily for further manipulation and plotting. It only keeps the measurements of temperature, resistivity, Seebeck coefficient and power factor and converts the values to their commonly used units. Note that information is lost during this process, which is why the original files have to be kept. To further improve convenience, both programs should be combined to reduce the amount of steps, which have to be taken.

Low-temperature resistivity measurements can also be performed using a separate measuring device, which is cooled with liquid helium. The measuring temperature can be brought down to about 2 K by reducing the pressure of the liquid helium using a rotary pump. The device has slots for two samples and uses the four-point method.

9 Results

9.1 Bulk Measurements

The aim of this work is to investigate the transport properties of off-stoichiometric Fe_2VAl bulk and thin film samples with the compositions $(\text{Fe}_{2/3}\text{V}_{1/3})_{75+x}\text{Al}_{25-x}$. Four 35 g samples with $x = \{-4, -3, 3, 4\}$ are produced from pure elements, as discussed in section 6. To ensure the proper compositions are adhered to and that the right phases formed, parts of the sample were pulverized in a mortar and measured using XRD-spectroscopy. Figure 9.1 shows XRD patterns of the four bulk samples. The theoretical Heusler peaks are shown at the bottom. The peak positions of all measurements correlate to Heusler peaks. The relative intensities vary, especially for the $(\text{Fe}_{2/3}\text{V}_{1/3})_{72}\text{Al}_{28}$ sample, yet no unwanted phase or contamination can be detected. Due to the off-stoichiometry, disorder is inherent in all samples. Possibly, the disorder is increased by crystallographic defects. Determining the crystal structure is difficult, as the relevant peaks have very low relative intensities. Nonetheless, B2-type disorder can be assumed due to the low intensity of the peak at 27° with respect to the intensity of the peak at 31° .

The lattice parameter a can be evaluated from the peak positions. Table 1 shows a for all four samples. Generally, a higher amount of Aluminium corresponds to a lower lattice parameter compared to the theoretical value of 5.763 \AA for stoichiometric $(\text{Fe}_{2/3}\text{V}_{1/3})_{75+x}\text{Al}_{25-x}$. The higher value of the $(\text{Fe}_{2/3}\text{V}_{1/3})_{72}\text{Al}_{28}$ sample indicates a higher amount of disorder in the sample, which was already indicated by the relative intensities of the diffraction peaks.

Subsequently, the thermoelectric properties are measured. Figure 9.2a shows the resistivity of the four compositions and of stoichiometric Fe_2VAl as a function of temperature. One can clearly see large values of the $(\text{Fe}_{2/3}\text{V}_{1/3})_{71}\text{Al}_{29}$ sample compared to the others. The resistivity of the samples $(\text{Fe}_{2/3}\text{V}_{1/3})_{71}\text{Al}_{29}$ and $(\text{Fe}_{2/3}\text{V}_{1/3})_{72}\text{Al}_{28}$ is also measured in a low-temperature measuring device. Figure 9.2b shows a combined graph of the resistivity as a function of temperature for the $(\text{Fe}_{2/3}\text{V}_{1/3})_{71}\text{Al}_{29}$ and $(\text{Fe}_{2/3}\text{V}_{1/3})_{72}\text{Al}_{28}$ samples. The high-temperature data are scaled to match the progression of the low-temperature data by about 10% using a linear fit. The high resistivity of the $(\text{Fe}_{2/3}\text{V}_{1/3})_{71}\text{Al}_{29}$ sample is confirmed by the low-temperature measurement. The absolute values of high-temperature and low-temperature measurement differ, yet the

	$(\text{Fe}_{2/3}\text{V}_{1/3})_{79}\text{Al}_{21}$	$(\text{Fe}_{2/3}\text{V}_{1/3})_{78}\text{Al}_{22}$	$(\text{Fe}_{2/3}\text{V}_{1/3})_{72}\text{Al}_{28}$	$(\text{Fe}_{2/3}\text{V}_{1/3})_{71}\text{Al}_{29}$
a [\AA]	5.77	5.78	5.78	5.76

Table 1. Lattice parameter a of $(\text{Fe}_{2/3}\text{V}_{1/3})_{75+x}\text{Al}_{25-x}$ samples.

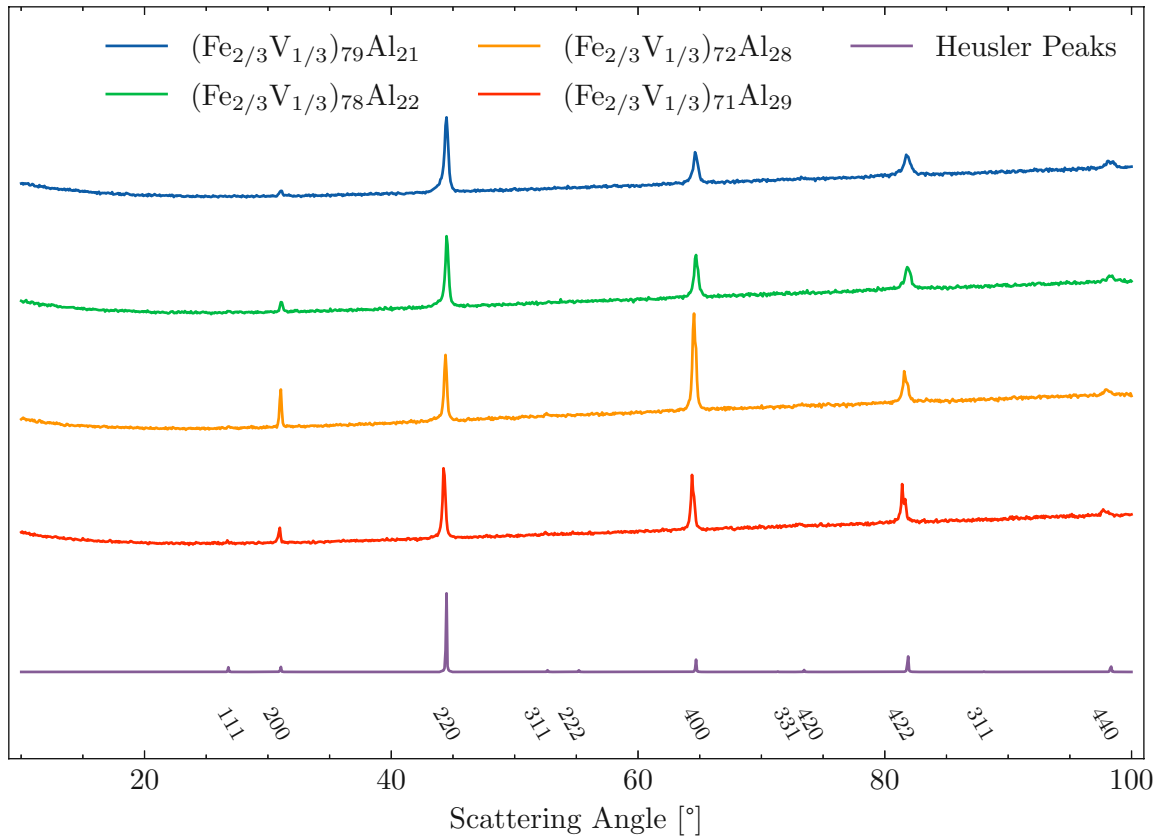


Figure 9.1. XRD-patterns of four samples of $(\text{Fe}_{2/3}\text{V}_{1/3})_{75+x}\text{Al}_{25-x}$ compounds. The positions of the expected Heusler peaks are shown at the bottom.

slopes at the junctions fit very well.

One can observe a rather complicated overlay of semi-conducting and metallic features in all substituted samples, with a declining resistivity for very small temperatures, an increase in the mid-temperature range and ultimately a decrease again as intrinsic conduction takes over. The progression of the stoichiometric sample is different as it shows intrinsic semi-conducting behavior. The high resistivity of the $(\text{Fe}_{2/3}\text{V}_{1/3})_{71}\text{Al}_{29}$ sample could result from changes in the band structure due to the off-stoichiometry and a shift of the Fermi energy. However, the similar curve progression with a constant offset suggests an added resistivity, which might come from cracks in the sample.

Figure 9.2c shows the Seebeck coefficient of the four samples as a function of temperature from room temperature to about 700 K. The sign of S is clearly determined by the offstoichiometry. The samples with $(\text{Fe}_{2/3}\text{V}_{1/3})_{72}\text{Al}_{28}$ and $(\text{Fe}_{2/3}\text{V}_{1/3})_{71}\text{Al}_{29}$, relating to a higher amount of aluminum, have a positive Seebeck coefficient and vice versa. This can be explained by the valence electron concentration, which is the number of valence electrons per atom. With 8 valence electrons of Fe, 5 of V and 3 of Al, the VEC of stoichiometric Fe_2VAl is 6.0. By introducing more elements with less valence electrons, the VEC decreases and vice versa. The VEC of the samples $(\text{Fe}_{2/3}\text{V}_{1/3})_{72}\text{Al}_{28}$,

$(\text{Fe}_{2/3}\text{V}_{1/3})_{71}\text{Al}_{29}$, $(\text{Fe}_{2/3}\text{V}_{1/3})_{78}\text{Al}_{22}$ and $(\text{Fe}_{2/3}\text{V}_{1/3})_{79}\text{Al}_{21}$ are 5.88, 5.84, 6.12 and 6.16, respectively. As discussed in section 3, this shifts the Fermi energy, or in other words, the absence of electrons leads to electron hole conduction, which results in a positive Seebeck coefficient. The absolute values of all samples are improved compared to their stoichiometric counterpart and the $(\text{Fe}_{2/3}\text{V}_{1/3})_{78}\text{Al}_{22}$ sample exceeds $-100 \mu\text{V K}^{-1}$ at its maximum. The similar curves of the $(\text{Fe}_{2/3}\text{V}_{1/3})_{72}\text{Al}_{28}$ and $(\text{Fe}_{2/3}\text{V}_{1/3})_{71}\text{Al}_{29}$ samples suggest cracks in the $(\text{Fe}_{2/3}\text{V}_{1/3})_{71}\text{Al}_{29}$ sample, which alter the resistivity but leave S unchanged. The stoichiometric sample has a Seebeck coefficient of about $25 \mu\text{V K}^{-1}$ at room temperature, which is also found in [7]. Figure 9.2d shows the power factors of the samples, which span from about 0.75 mW/m K^2 to about 2.5 mW/m K^2 . All off-stoichiometric samples have a higher power factor than Fe_2VAl due to their higher Seebeck coefficient and similar resistivities.

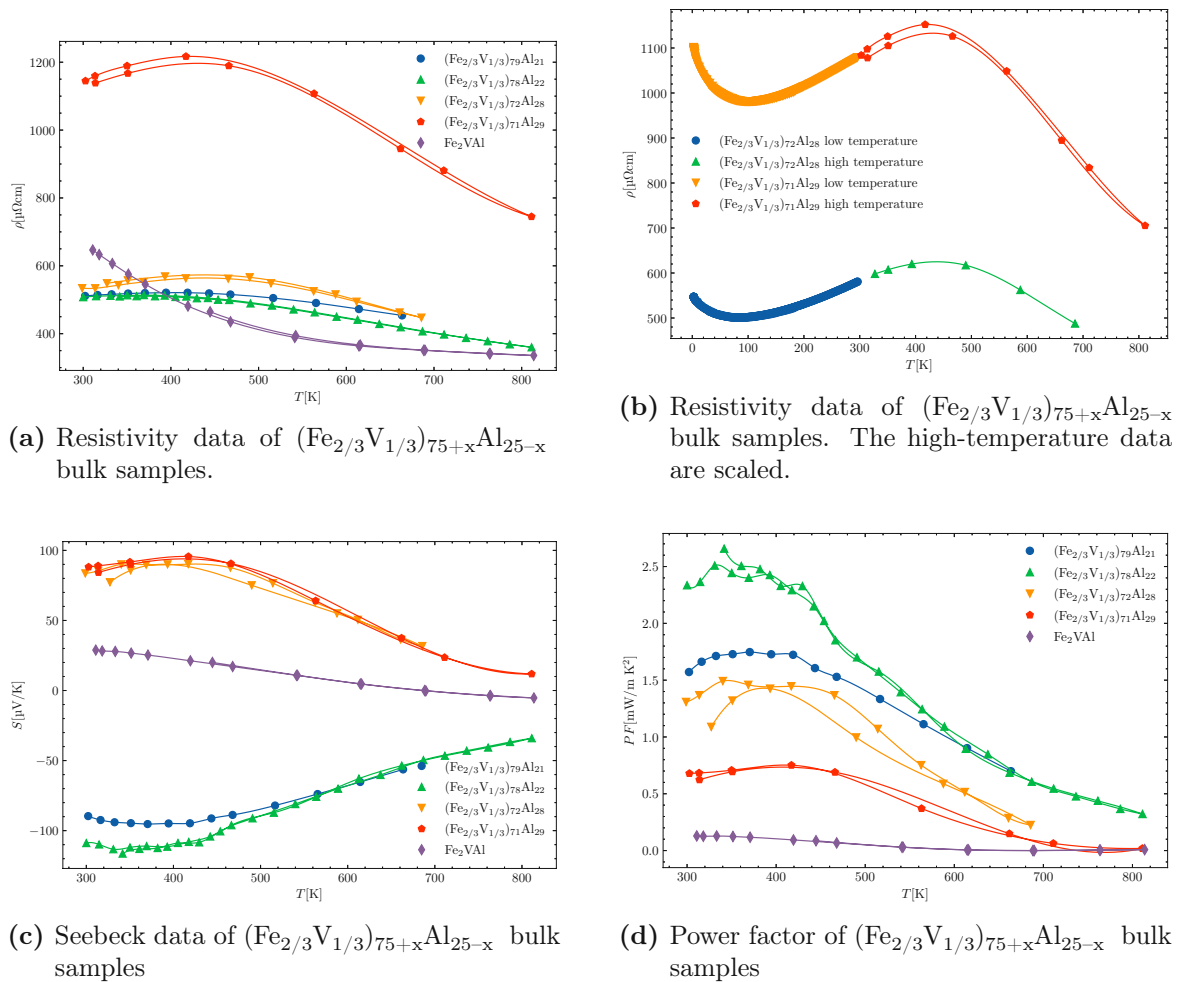


Figure 9.2. Thermoelectric properties of $(\text{Fe}_{2/3}\text{V}_{1/3})_{75+x}\text{Al}_{25-x}$ bulk samples.

9.2 Silicon Substrate

In this work, thin films are produced on silicon substrates. These wafers, with a thickness of $279 \pm 25 \mu\text{m}$, have high electrical resistivities, which diminishes their influence on thin films. The wafers are produced using the Czochralski method by SIEGERT WAFER GmbH. Single-side polished and double-side polished wafers are used as sputtering substrates. Mostly, undoped wafers are employed but for some measurements, boron-doped p-type wafers are used as well.

To estimate the wafers' influence on a substrate-film system, resistivity and Seebeck measurements are performed on three undoped and one p-doped wafers. After thin films are produced, they are often annealed. To simulate this process, silicon wafers are annealed as well at 450°C for seven days and subsequently measured. Figure 9.3 shows the resistivity data from the measurements before and after annealing as obtained from ZEM 3. The unannealed wafers show high resistivities of about $10^7 \mu\Omega\text{cm}$ with a maximum at around 500 K. The annealed wafers, however, have resistivities which are two orders of magnitude smaller. This effect arises due to oxygen contamination in silicon, which leads to thermal donors being generated when annealing the crystal below 500°C [17]. Oxygen is embedded within the silicon during the production process, when using the Czochralski method [30]. The resistivity of p-doped silicon is slightly smaller than the one of undoped silicon. For high temperatures, the resistivities converge for all samples.

The Seebeck measurements in figure 9.4a give values of about $-1,000 \mu\text{V K}^{-1}$ at 400 K for annealed and not-annealed wafers. The latter show a different behavior compared to their counterparts. Figure 9.4b shows the Seebeck coefficient of the not-annealed undoped wafers and of the p-doped wafer. The latter has a positive Seebeck coefficient of about $1,000 \mu\text{V K}^{-1}$, which decrease for higher temperatures and becomes negative at about 600 K.

Contrary to other measurements, the silicon wafers have to be measured from high temperatures to low temperatures and cannot be measured at temperatures smaller than about 350 K. Probably, this is due to their very high resistivities at room temperature. Considering this fact, the high rise of S for low temperatures in figure 9.4a has to be regarded with care, especially, as it is only seen for one sample.

The drop of the wafers' resistivity after annealing might lead to measurement errors, if this effect is not considered. However, the used measuring device is not fitting for this kind of high resistivity measurements, which leads to varying graphs in figure 9.3. Careful high resistivity measurements should be conducted to further evaluate this effect.

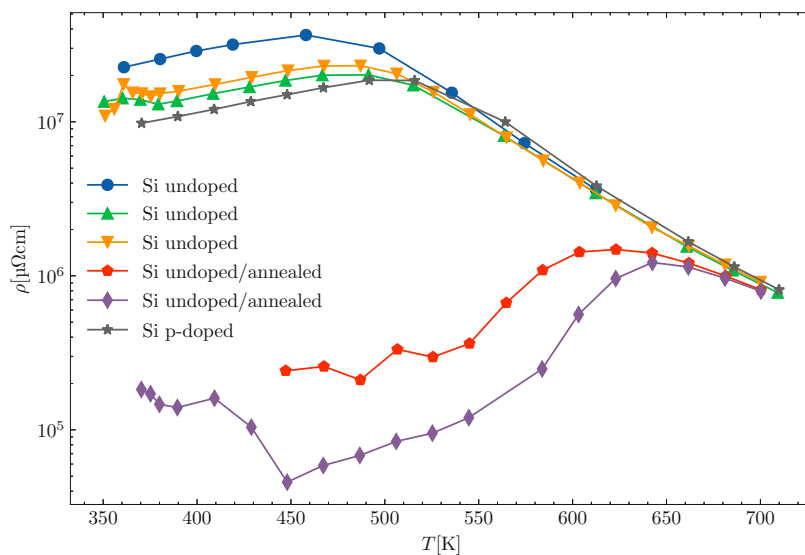
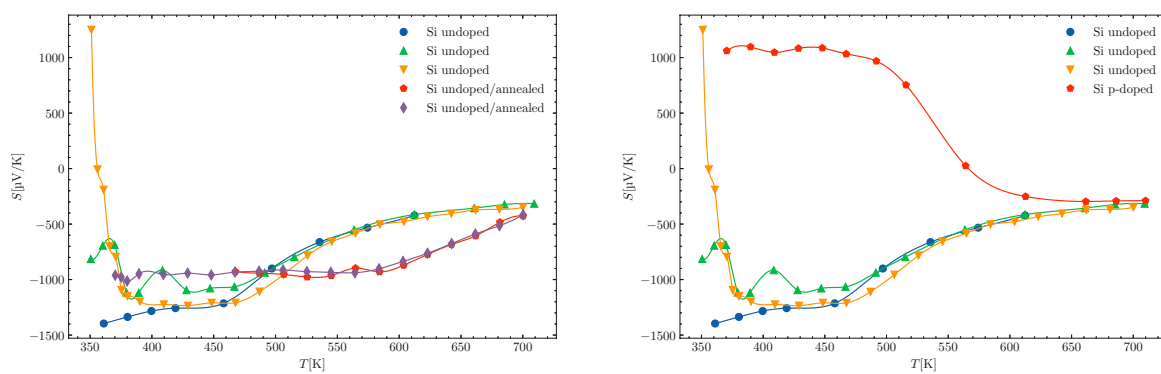


Figure 9.3. Resistivity data of undoped and p-doped silicon wafers, which were produced using the Czochralski method. The wafers were annealed for seven days at 450 °C.



(a) Seebeck measurements of undoped Silicon wafers before and after annealing.

(b) Seebeck measurements of undoped and p-doped Silicon wafers before annealing.

Figure 9.4. Si Wafers.

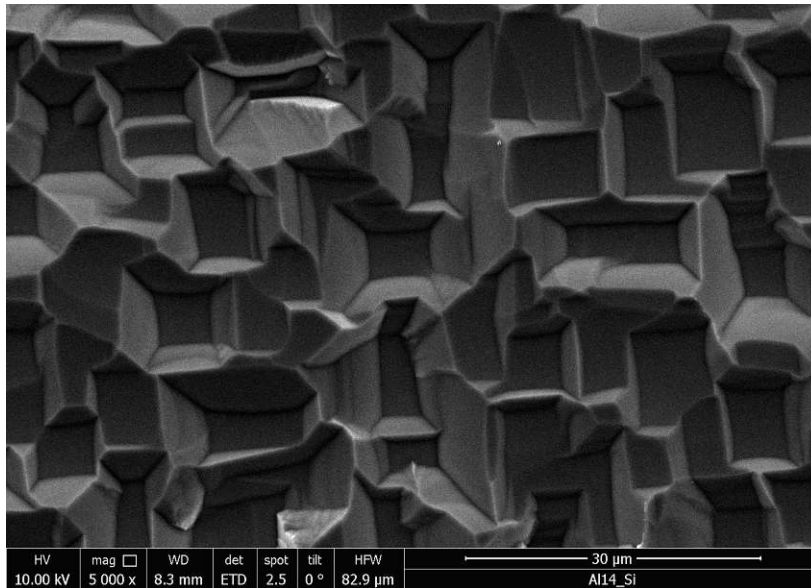


Figure 9.5. SEM measurement of an unpolished undoped silicon wafer.

Figure 9.5 shows an unpolished silicon wafer. The image was made with a scanning electron microscope at a magnification of 5000x. The surface is characteristic for silicon with visible geometric shapes. The dimensions of these shapes are large compared to the films which are coated on top. The sputtered films detach a lot less from unpolished wafers than from polished ones.

9.3 Thin Film Measurements

Thin films are produced from the $(\text{Fe}_{2/3}\text{V}_{1/3})_{72}\text{Al}_{28}$ sample with a sputtering current of 0.07 A and 25 W. Polished and unpolished silicon substrates are used, which are heated to 500 °C during sputtering. The films are heat treated afterwards for seven days at 450 °C. Figure 9.6 shows resistivities and Seebeck coefficients of four films, which are produced in two separate synthesis series. Figure 9.6a shows the resistivities of two films with thicknesses of 0.5 μm and 1 μm . The two curves match very well. The measured resistivities are higher compared to the bulk samples. Figure 9.6b shows the resistivities of two other samples. The film thicknesses could not be measured properly, because the test samples' films detached from the substrate. The films had to be estimated to have a thickness of 0.25 μm and 0.5 μm , respectively. Therefore, the absolute values of this graph have to be considered with caution. Furthermore, the samples are produced on different slots on the substrate holder, which turned out to have different sputter rates. Nonetheless, the sample on unpolished silicon has been sputtered twice as long as its counterpart on polished silicon and its thickness is roughly twice as large.

Figures 9.6c and 9.6d show the Seebeck coefficients of the films discussed. All four samples show negative values over the whole temperature range, whereas the bulk's Seebeck has a positive sign. The samples with thicker films seem to have lower absolute values but this is not evident, due to the large insecurities of the thickness measurements.

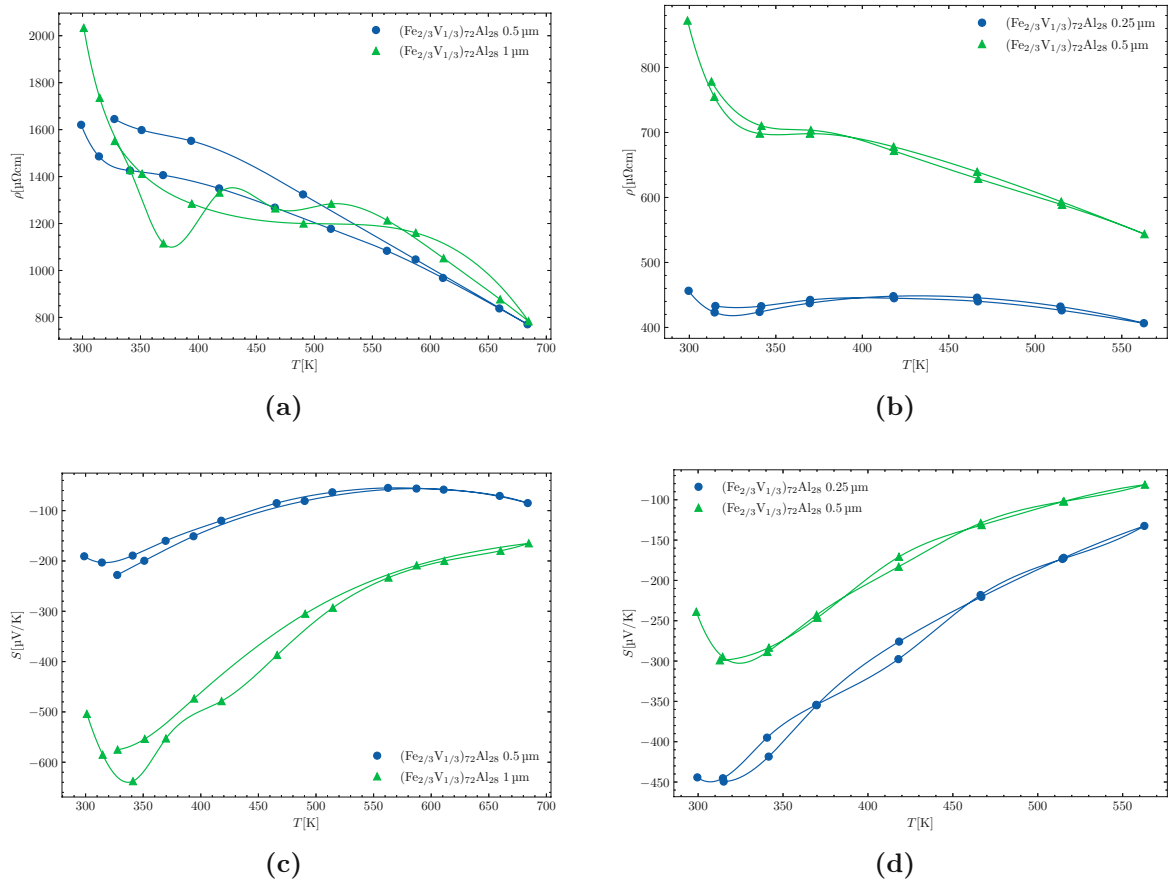


Figure 9.6. Resistivity and Seebeck measurements of $(\text{Fe}_{2/3}\text{V}_{1/3})_{72}\text{Al}_{28}$ thin films on silicon substrates after annealing for seven days at 450°C .

9.4 Scraped-off Film

To further investigate the correlation of film thickness and Seebeck coefficient, a sample with a $0.5 \mu\text{m Fe}_2\text{V}_{0.8}\text{W}_{0.2}\text{Al}$ film on a silicon substrate is heat treated for five days at 450°C . Afterwards, its film is carefully removed using sandpaper to inspect a possible intermediate layer.

Figure 9.7 shows the electrical resistivity of the sample before and after annealing and after removing the film as a function of temperature. The resistivity rises to about $500 \mu\Omega \text{ cm}$ after annealing. This cannot be explained by the influence of the substrate, as its resistance should be lower after heat treatment. Possibly, the film's resistance rises due to cracks after thermal expansion. After removing the film, however, the resistivity's slope is much larger for temperatures above room temperature and the graph features a different behavior, yet the resistivity is orders of magnitude lower than the one measured in pure silicon wafers.

The Seebeck coefficient, rises distinctly after annealing and exceeds $-1,000 \mu\text{V K}^{-1}$ after the film is removed, as seen in figure 9.8. This means that the power factor $\frac{S^2}{\rho}$ reaches 200 mW/m K^2 at room temperature, see figure 9.9.

The interpretation of these data is not easy, as changes in the film, the substrate and the combination of both can play a role. A possible explanation for the rise in S after heat treatment can be given by the substantial decrease in resistivity of the silicon substrate, which was discussed in section 9.2. As an example, the resistivities of substrate and film are calculated using equations 7.5 and 7.12. As input parameters the Seebeck coefficient of silicon is taken from figure 9.4a and set to $-1,250 \mu\text{V K}^{-1}$ before annealing and $-1,000 \mu\text{V K}^{-1}$ afterwards. The Seebeck coefficient of the film is arbitrarily set to $5 \mu\text{V K}^{-1}$. The total resistivity and Seebeck coefficient is taken from figure 9.7 and 9.8. All data are taken at 420 K as no low temperature silicon data are available.

	ρ_F	ρ_S
before annealing	$193 \mu\Omega \text{ cm}$	$1.6 \times 10^7 \mu\Omega \text{ cm}$
after annealing	$752 \mu\Omega \text{ cm}$	$1.1 \times 10^6 \mu\Omega \text{ cm}$

Table 2

This is only an example as unsupported assumptions about the film's Seebeck coefficient are made. Nonetheless, this calculation shows negligible influence of the substrate before annealing, which becomes important, after a drop in resistivity, which fits the data in figure 9.3.

The Seebeck measurement after removing the film is similar to the one of pure silicon,

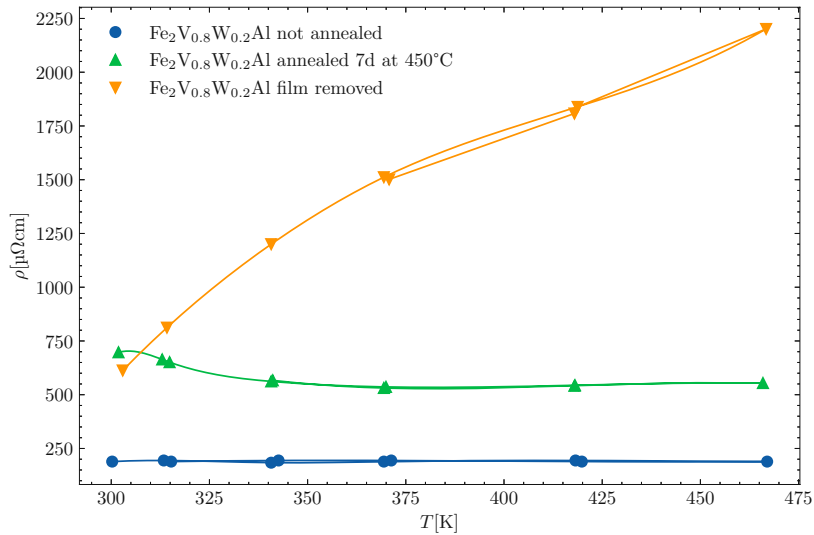


Figure 9.7. Electrical resistivity of a 0.5 μm $\text{Fe}_2\text{V}_{0.8}\text{W}_{0.2}\text{Al}$ film before and after annealing and after removing the film.

yet the resistivity is orders of magnitude smaller, which results in a very high power factor. To investigate the origin of these results, a new test series is started, with more control over the film thickness, as well as the thermoelectric properties.

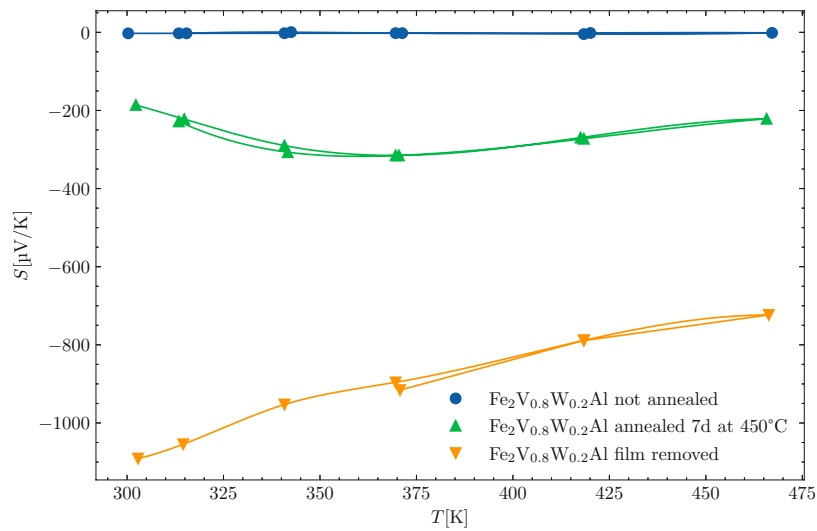


Figure 9.8. Seebeck coefficient of a $0.5 \mu\text{m}$ $\text{Fe}_2\text{V}_{0.8}\text{W}_{0.2}\text{Al}$ film before and after annealing and after removing the film.

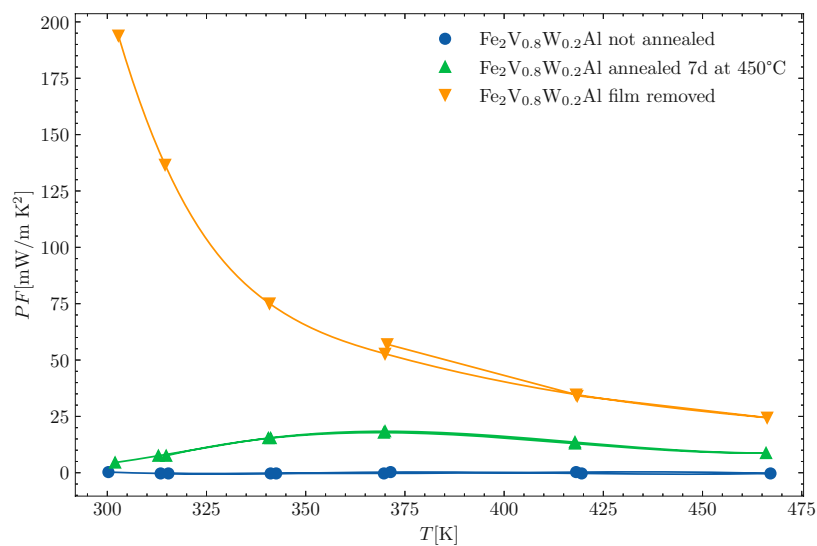


Figure 9.9. Power Factor of a $0.5 \mu\text{m}$ $\text{Fe}_2\text{V}_{0.8}\text{W}_{0.2}\text{Al}$ film before and after annealing and after removing the film.

9.5 Aluminium Films

Trying to recreate the results from section 9.4 with the least amount of variables possible, thin films from pure aluminium are produced on undoped silicon substrates. Seven samples are prepared with film thicknesses from 0.05 μm to 0.6 μm . Another film with a thickness of 0.01 μm is produced but cannot be measured because the electrical resistance is too large.

The left graph in figure 9.10 shows the electrical resistivity as a function of temperature. All data points are of the order of $10 \mu\Omega \text{cm}$ and the data sets are roughly in the order of their film thickness. The rising electrical resistivity with decreasing film thickness cannot be explained with the influence of the substrate. Using equation 7.5 with approximate values for the resistivities of film ($10 \mu\Omega \text{cm}$) and substrate ($10^7 \mu\Omega \text{cm}$), the relative error made by neglecting the substrate is less than 0.1 %.

On the left of figure 9.11 one can see the Seebeck coefficient as a function of temperature. $-2 \mu\text{V K}^{-1}$ at room temperature with decreasing values for higher temperatures is in agreement with the data in [8]. Interestingly, the 0.05 μm film shows a steeper slope and a hysteresis when cooling down.

After measurement, the samples are annealed at 450°C for seven days and the resistivity and the Seebeck coefficient are measured again. The right graph in figure 9.10 shows the electrical resistivity after annealing. The comparison of left and right graph shows no significant change after annealing. The graph of the Seebeck coefficient in figure 9.11 shows no significant changes either, although the absolute value exceeds $10 \mu\text{V K}^{-1}$ and there are few positive values. This indicates that the influence of the substrate is rising but still is insignificant due to the large conductivity of aluminium.

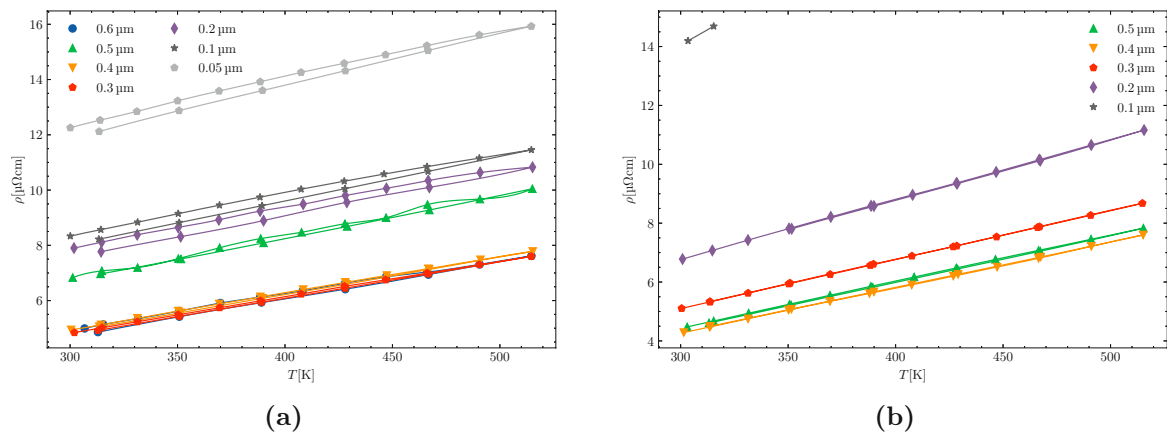


Figure 9.10. (a): Electrical resistivity of various Al-films on silicon substrates before annealing; (b): Electrical resistivity of various Al-films on silicon substrates after annealing at 450°C for seven days.

To further investigate very thin films, the 0.05 μm film is etched three times, twice

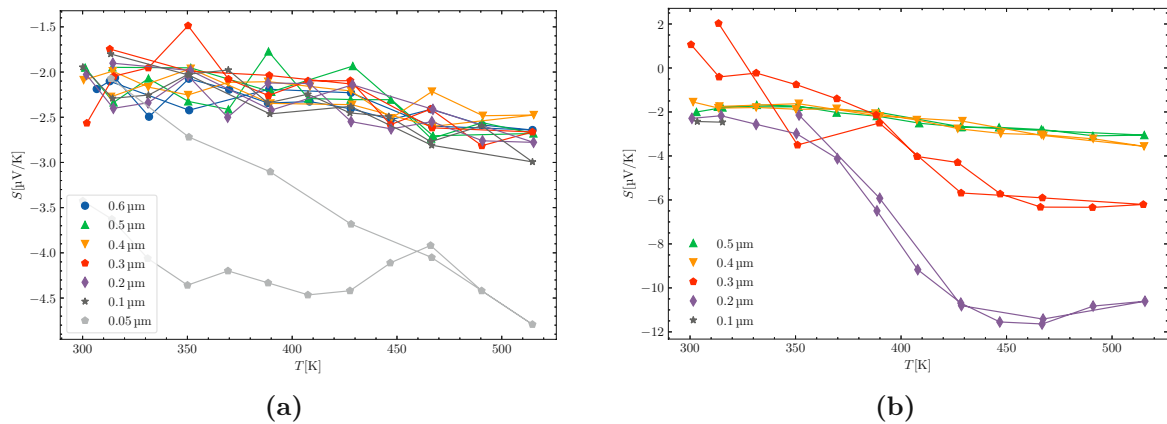


Figure 9.11. (a): Seebeck coefficient of various Al-films on silicon substrates before annealing; (b): Seebeck coefficient of various Al-films on silicon substrates after annealing at 450 °C for seven days.

for 30 seconds and once for one minute. The results can be seen in figure 9.12. The left graph shows measurements of the same sample with resistivities about ten times larger than before etching. The right graph shows the Seebeck coefficients. Values up to $-900 \mu\text{V K}^{-1}$ are far greater than can be explained by aluminium films and are only possible due to the influence of the substrate. The low resistivity values together with high values of S look promising but are erroneous. As the influence of the substrate rises, the resistivity of the film cannot be calculated as before but has to be carefully analyzed.

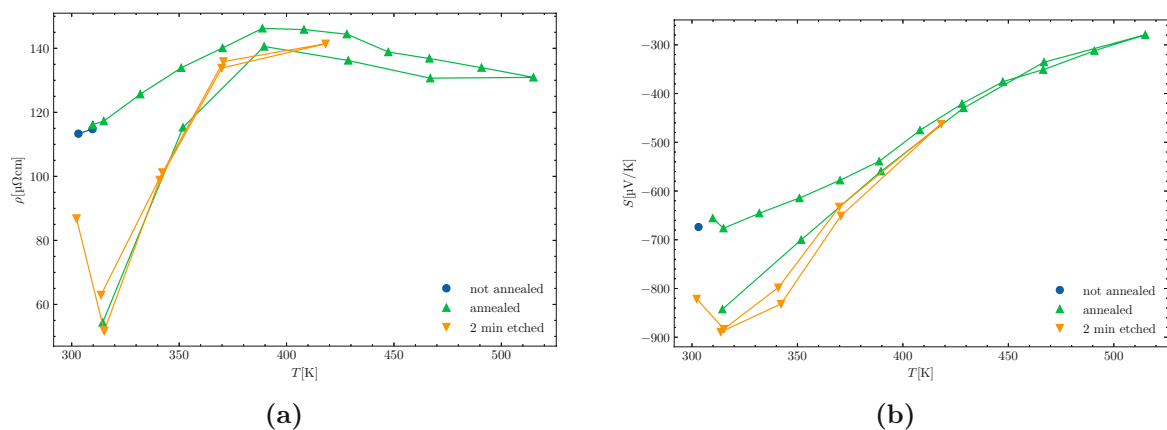


Figure 9.12. (a): Electrical resistivity of a 0.05 μm Al-films on a silicon substrate after annealing and 2 min etching; (b): Seebeck coefficient of a 0.05 μm Al-films on a silicon substrate after annealing and 2 min etching.

9.6 Chromium Films

For another test series, chromium targets are manufactured, which are again sputtered on silicon wafers. For comparison, different substrates are used. The films are produced on undoped silicon wafers and on p-doped wafers and are not heat treated. The film

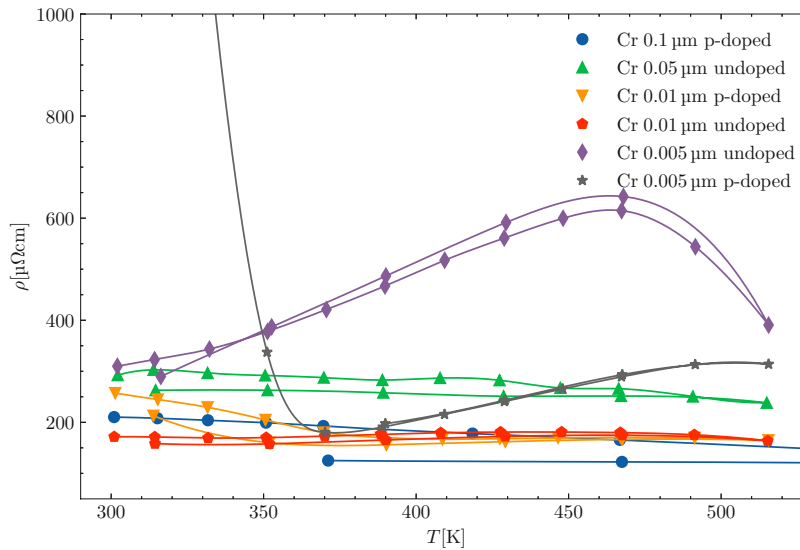


Figure 9.13. Resistivity measurements of Chromium films with varying thicknesses on silicon substrates.

thicknesses range from 0.1 μm to 0.005 μm . Figure 9.13 shows the electrical resistivity of the films. The resistivities are roughly rising with lower film thicknesses, while the 0.005 μm p-doped sample reaches 2,700 $\mu\Omega\text{cm}$ at room temperature. Figure 9.14 shows the Seebeck coefficient of the chromium films. It ranges from $-1,000\ \mu\text{V K}^{-1}$ to $1,000\ \mu\text{V K}^{-1}$. The films on p-doped silicon have positive values and the ones on undoped silicon have negative values. This result is not surprising considering the high Seebeck coefficient of silicon, as seen in figure 9.4b. The dopant-dependent sign demonstrates the influence of the substrate.

The same calculations as in section 9.4 can be performed here using the data from figure 9.13 and 9.14 at 420 K. At this temperature, the Seebeck coefficient of chromium is $17\ \mu\text{V K}^{-1}$ [22]. Table 3 shows similar values for undoped and p-doped samples. The steep rise of the film resistivity for the 0.005 μm films indicates the low influence of the film on the total measurement. Due to the small thickness, the film might even be discontinuous, which is why the Seebeck coefficient is as high as the one of pure silicon. The relatively low measured resistivity of these samples has to be questioned. In fact, the resistivity of thin films is usually calculated by dividing the resistance by the film's dimensions. If the substrate has a non negligible influence, the calculated resistivity is erroneous as was discussed in section 7. In this extreme case, the film has no influence any more and the resistivity of the substrate can be found by dividing the data by the film's thickness and multiplying with the substrate's thickness. Doing so, resistivity values in the range of $10^7\ \mu\Omega\text{cm}$ emerge, which fit silicon wafers.

The calculated film resistivities of $200\ \mu\Omega\text{cm}$ to $300\ \mu\Omega\text{cm}$ are large compared to the resistivity of bulk chromium. Possible explanations are a higher resistivity due to

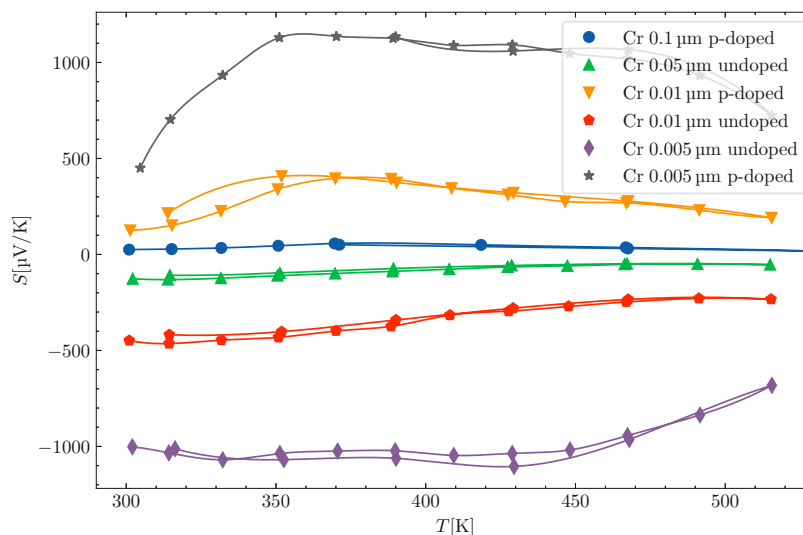


Figure 9.14. Seebeck measurements of Chromium films with varying thicknesses on silicon substrates.

	undoped			p-doped		
film thickness	0.05	0.01	0.005	0.05	0.01	0.005
ρ_F	282	231	3871	295	238	3998
ρ_S	2.47×10^7	1.98×10^7	3.59×10^7	2.26×10^7	1.54×10^7	1.37×10^7

Table 3. Calculation of film and substrate resistivities of chromium films on silicon substrates.

scattering on the film's boundaries and grain boundaries, the latter being increased by sputtering, as well as by an overestimation of the film's thickness. As the films are very thin, discontinuous coating and inhomogeneities might lead to wrong results. In this case, the simple model of two parallel bars is not applicable anymore, as the current can only move on specific paths. Therefore, samples with greater film thicknesses are recommended to avoid such complications.

9.7 Fe₂VAl-Films

To demonstrate the substrate influence on Heusler films, stoichiometric Fe₂VAl films on undoped silicon wafers are produced. Six films are sputtered, three of which have a thickness of 0.5 μm and the rest has a thickness of 1 μm. Each batch is produced in the same sputtering process. After measuring their thermoelectric properties, the films are annealed for seven days at 450 °C and measured again.

Figure 9.15a shows the resistivity of all six films before annealing. Contrary to the prior plots, in this case the resistivity of the substrate-film system is given, which is calculated by dividing the measured resistance by the dimensions of film and substrate

put together. The high resistivities of the 0.5 μm films cannot be explained by the influence of the substrate. Again, as the resistivity is very high, this is most probably caused by a discontinuous film.

Figure 9.15b shows the total Seebeck coefficient of the measured films. The large absolute values of S are not surprising if the resistivity values of the substrate-film system and the high Seebeck coefficient of silicon are taken into account. For the 1 μm films, the substrate has very little influence, as the Seebeck coefficient is only slightly negative.

Figure 9.16a and figure 9.16b show resistivity and Seebeck coefficient of the 0.5 μm annealed and not annealed films. The annealed films have a very high resistivity, which does not fit the data of the measured silicon wafers. The not annealed wafers showed values up to $10^7 \mu\Omega \text{cm}$ which went down after annealing. It seems as though these wafers have even higher resistivities. The fact that the total resistivity rises after annealing is not expected and might be due the film not sticking to the substrate, which increases the mentioned effect. The Seebeck coefficient goes down to $-1,300 \mu\text{V K}^{-1}$ which might be just the substrate being measured.

Figure 9.17a and 9.17b show resistivity and Seebeck coefficient of the 1 μm batch before and after annealing. The resistivity rises after annealing, which means that the resistivity of the substrate, the film or both have to rise. If one assumes the silicon wafer's resistivity to drop when annealing, the film's resistivity has to rise. The Seebeck data imply this behavior, as it shows values close to zero for the not annealed wafers, which go down to $-300 \mu\text{V K}^{-1}$ after annealing. This might be due to the substrate gaining influence.

Calculating the substrate's and the film's part of the total resistivity is again possible with equations 7.5 and 7.12. Without the necessary measurements, the Seebeck coefficient of the silicon wafers is estimated to be $-1,300 \mu\text{V K}^{-1}$, which is the minimum in figure 9.16b and the one of Fe_2VAI is set to $25 \mu\text{V K}^{-1}$. Again, possible changes during annealing are omitted. Figure 9.18 shows the estimated resistivities of the film and the substrate. The calculation leads to a resistivity of the film of about $10^3 \mu\Omega \text{cm}$ which is in accordance with the expected values. The substrate has a resistivity of $10^7 \mu\Omega \text{cm}$ and $10^6 \mu\Omega \text{cm}$ after annealing. The film's resistivity rises after annealing. Again, these are not accurate values, as changes in the film's or the substrate's Seebeck coefficient would lead to other results. This shall only show, how a drop in the wafer's resistivity would lead to the measured results.

The rise of the films's resistivities after annealing is not expected. On the contrary, heat treatment should lead to a rearrangement of the atoms into a more ordered crystal

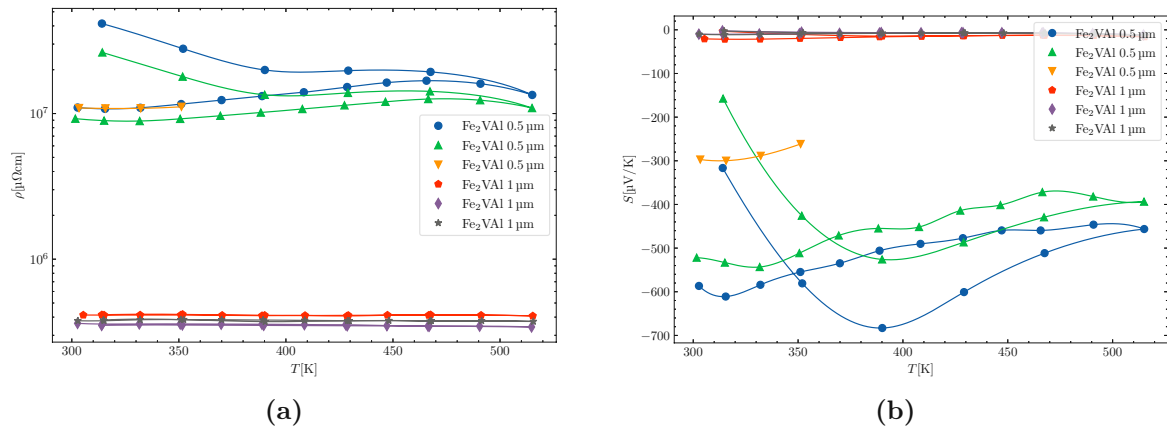


Figure 9.15. (a): Resistivity measurements of not annealed 0.5 μm and 1 μm Fe_2VAI films on silicon substrates; (b): Seebeck measurements of not annealed 0.5 μm and 1 μm Fe_2VAI films on silicon substrates.

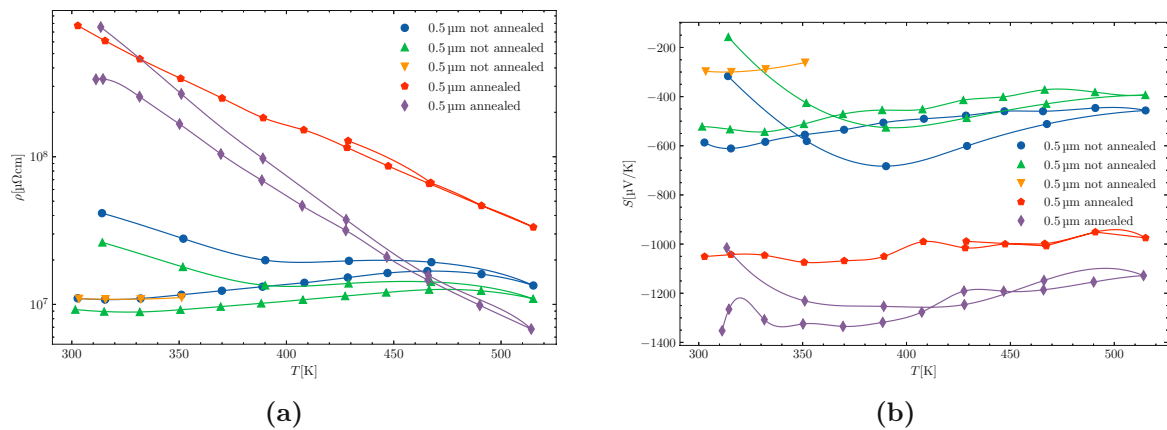


Figure 9.16. (a): Resistivity measurements of 0.5 μm Fe_2VAI films on silicon substrates before and after annealing; (b): Seebeck measurements of 0.5 μm Fe_2VAI films on silicon substrates before and after annealing.

structure and consequently a lower resistivity. Therefore, further measurements should be conducted to understand the unusual resistivity behavior upon annealing and make a clear statement about the substrate's influence.

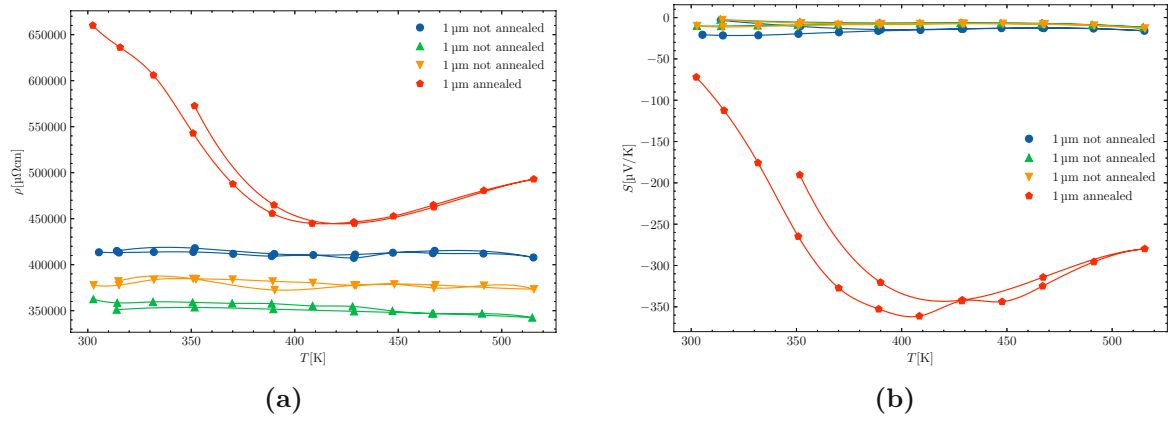


Figure 9.17. (a): Resistivity measurements of 1 μm Fe_2VAl films on silicon substrates before and after annealing; (b): Seebeck measurements of 1 μm Fe_2VAl films on silicon substrates before and after annealing.

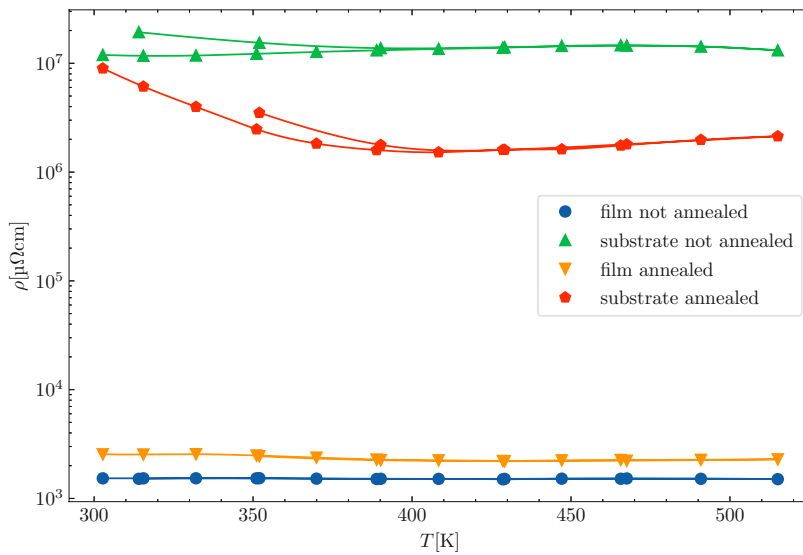


Figure 9.18. Resistivity contributions of a Si substrate and a 1 μm Fe_2VAl film, calculated from the measured data in figures 9.16a and 9.16b.

10 Conclusio

After producing and measuring off-stoichiometric $(\text{Fe}_{2/3}\text{V}_{1/3})_{75+x}\text{Al}_{25-x}$ bulk and film samples, attention was given to the thin film manufacturing process. A theoretical expression for the sputtering intensity is derived, which is then used to adjust the sputtering device. Great efforts are put into implementing sputter etching as well as magnetron sputtering in the same vacuum chamber. Although sputter etching works, accurate etching rates have yet to be determined.

The second part of this work treats the influence of silicon substrates on the thermoelectric properties of thin films. Equations for the total resistivity and Seebeck coefficient substrate-film systems are obtained, which are then used to calculate each partial quantity.

Measurements of silicon wafers show a drop in resistivity when annealed at 450 °C in agreement with literature. This effect may lead to misunderstandings, when annealing films on silicon substrates. Subsequently, chromium and aluminium films are produced, which unsurprisingly show high values of S , if their thickness is small enough, therefore the resistance increases. Disregarding the influence of the substrate, may, however, lead to the assumption of low resistivities and high values of the Seebeck coefficient at the same time.

To further investigate this effect, Fe_2VAl films on silicon wafers were measured. 1 μm thick films show no relevant thermoelectric properties, whereas the ones with 0.5 μm do. After annealing, the absolute values of the Seebeck coefficient rise for all samples. However, ascribing the measured properties to the film alone would lead to wrong results as the influence of the silicon substrate can not be neglected. Still, discontinuous films make a quantitative assessment difficult and further measurements are required.

The performed measurements show the importance of careful analysis when dealing with substrate-film systems, especially when using silicon as a substrate.

References

- [1] H. Adachi and K. Wasa. “Thin Films and Nanomaterials”. In: *Handbook of Sputtering Technology (Second Edition)*. Ed. by K. Wasa, I. Kanno, and H. Kotera. Second Edition. Oxford: William Andrew Publishing, 2012, pp. 3–39.
- [2] N. W. Ashcroft and D. N. Mermin. *Festkörperphysik*. ger. 4., verb. Aufl.. München: Oldenbourg, 2013.
- [3] L. Chen, R. Liu, and X. Shi. “General principles of thermoelectric technology”. In: *Thermoelectric Materials and Devices*. Ed. by L. Chen, R. Liu, and X. Shi. Elsevier, 2021, pp. 1–18.
- [4] W. Demtröder. *Experimentalphysik 2 : Elektrizität und Optik*. ger. 5th ed. Springer-Lehrbuch. Berlin, Heidelberg: Springer Berlin Heidelberg, 2009.
- [5] W. Demtröder. *Experimentalphysik 4: Kern-, Teilchen- und Astrophysik*. ger. 4. Aufl. 2014. Springer-Lehrbuch. Berlin, Heidelberg: Springer Berlin Heidelberg.
- [6] C. Gayner and K. K. Kar. “Recent advances in thermoelectric materials”. In: *Progress in Materials Science* 83 (2016), pp. 330–382.
- [7] T. Graf, C. Felser, and S. Parkin. “Simple rules for the understanding of Heusler compounds”. In: *Progress in Solid State Chemistry* 39.1 (2011), pp. 1–50.
- [8] R. J. Griphover, J. B. VanZytveld, and J. Bass. “Thermopower of Pure Aluminum”. In: *Phys. Rev.* 163 (3 Nov. 1967), pp. 598–603.
- [9] R. Gross and A. Marx. *Festkörperphysik*. 2., aktualisierte Auflage. Berlin [u.a.]: de Gruyter, 2014.
- [10] M. B. Heaney. “Electrical Conductivity and Resistivity”. In: *Measurement, Instrumentation, and Sensors Handbook*. Ed. by J. G. Webster and E. Halit. CRC Press, 2014.
- [11] F. Heusler. “Über magnetische Manganlegierungen”. German. In: *Verhandlungen der Deutschen Physikalischen Gesellschaft*. 1903.
- [12] B. Hinterleitner et al. “Stoichiometric and off-stoichiometric full Heusler Fe₂V_{1-x}W_xAl thermoelectric systems”. In: *Physical Review B* 102.7 (Aug. 2020).
- [13] B. Hinterleitner et al. “Thermoelectric performance of a metastable thin-film Heusler alloy”. In: *Nature* 576.7785 (Nov. 2019), pp. 85–90.
- [14] Institut für Festkörperphysik. *Metallische Verbindungen und Legierungen*. URL: <https://www.ifp.tuwien.ac.at/index.php?id=73> (visited on 10/20/2020).
- [15] H. Krieger. *Grundlagen der Strahlungsphysik und des Strahlenschutzes*. Wiesbaden: Teubner, 2007.
- [16] H. Lee. *Thermoelectrics: Design and Materials*. eng. New York: John Wiley & Sons, Incorporated, 2016.
- [17] C. A. Londos et al. “Effect of oxygen concentration on the kinetics of thermal donor formation in silicon at temperatures between 350 and 500 °C”. In: *Applied*

- Physics Letters* 62.13 (1993), pp. 1525–1526. eprint: <https://doi.org/10.1063/1.108628>.
- [18] D. M. Mattox. “Physical Sputtering and Sputter Deposition”. In: *The Foundations of Vacuum Coating Technology (Second Edition)*. Ed. by D. M. Mattox. Second Edition. William Andrew Publishing, 2018, pp. 87–149.
- [19] M. Mikami and K. Kobayashi. “Effect of Bi addition on microstructure and thermoelectric properties of Heusler Fe₂VAl-sintered alloy”. In: *Journal of Alloys and Compounds* 466.1 (2008), pp. 530–534.
- [20] M. Mikami et al. “Effect of Off-Stoichiometry on the Thermoelectric Properties of Heusler-Type Fe₂VAl Sintered Alloys”. In: *Journal of Electronic Materials* 45.3 (Aug. 2015), pp. 1284–1289.
- [21] M. Mikami, T. Kamiya, and K. Kobayashi. “Microstructure and thermoelectric properties of Heusler Fe₂VAl thin-films”. In: *Thin Solid Films* 518.10 (2010), pp. 2796–2800.
- [22] J. P. Moore, R. K. Williams, and R. S. Graves. “Thermal conductivity, electrical resistivity, and Seebeck coefficient of high-purity chromium from 280 to 1000 K”. In: *Journal of Applied Physics* 48.2 (1977), pp. 610–617. eprint: <https://doi.org/10.1063/1.323697>.
- [23] Y. Nishino. “Unusual electron transport in Heusler-type Fe₂VAl compound”. In: *Intermetallics* 8.9 (2000), pp. 1233–1241.
- [24] M. Ohring. “Chapter 3 - Thin-Film Evaporation Processes”. In: *Materials Science of Thin Films (Second Edition)*. Second Edition. San Diego: Academic Press, 2002, pp. 95–144.
- [25] N. M. Ravindra et al. *Thermoelectrics*. Springer International Publishing, 2019.
- [26] D. M. Rowe. “Thermoelectric Generators”. In: *Advances in Electronic Ceramics II*. John Wiley & Sons, Ltd, 2009, pp. 107–123. eprint: <https://ceramics.onlinelibrary.wiley.com/doi/pdf/10.1002/9780470584422.ch9>.
- [27] A. H. Simon. “Sputter Processing”. In: *Handbook of Thin Film Deposition (Fourth Edition)*. Ed. by K. Seshan and D. Schepis. Fourth Edition. William Andrew Publishing, 2018, pp. 195–230.
- [28] ULVAC. *ZEM-3*. Feb. 22, 2021. URL: <https://www.ulvac.eu/en/products/components/thermal-analysis/zem-3.html>.
- [29] Wolfram Research, Inc. *Mathematica, Version 12.0*. Champaign, IL, 2019.
- [30] W. Zulehner. “Czochralski growth of silicon”. In: *Journal of Crystal Growth* 65.1 (1983), pp. 189–213.

List of Figures

2.1	Model of a thermoelectric generator (TEG).	15
3.1	Periodic table highlighting the elements used for Heusler compounds [7].	17
3.2	Band structure of Fe_2VAl .	18
3.3	Seebeck coefficient of $\text{Fe}_2\text{V}_{1-x}\text{Al}_{1+x}$.	19
3.4	Density of states of Fe_2VAl .	20
4.1	X-rays reflected on lattice plains. The path difference is given by $2d \sin \theta$.	21
4.2	Bragg-Brentano diffractometer.	22
5.1	Setups for DC- and RF- sputtering [1].	23
5.2	Sputter yield as a function of ion energy for different target materials [27].	24
5.3	Used sputter target with ablation ring.	26
5.4	Substrate holder.	27
5.5	Angular distribution of a point source and a surface source, [24].	28
5.6	Parallel target-substrate geometry.	28
5.7	Ring-shaped target with parallel planar substrate.	29
5.8	Intensity distribution $I(x, y)$ with $y = 0$.	30
6.1	<i>left</i> : Hukin crucible with cut samples inside; <i>right</i> : Hukin crucible during melting.	31
6.2	Target holder without target. Inside the grounded shielding one can see the copper cylinder with circularly arranged magnets.	32
6.3	Target holder with target built in.	33
6.4	Inside of the vacuum chamber with built-in target holder.	33
6.5	Inside of the vacuum chamber with built-in substrate holder.	34
6.6	Vacuum cover with shutter mechanism.	34
6.7	Vacuum cover modified for the use of target holder and shutter.	35
6.8	Target holder with shutter in open position.	35
6.9	Using a profilometer to measure the film thickness of a sample.	36
6.10	Profile measurement.	36
6.11	Magnet holder.	38
6.12	Magnetic setup used for sputter etching.	38
6.13	Model of the vacuum chamber with the etching setup: magnet holder (top), substrate holder (mid) and target holder (bottom).	39
6.14	<i>left</i> : Substrate holder with a sharp edge above the sample; <i>right</i> : Nearly planar substrate holder.	39
6.15	<i>left</i> : Clamp with glass plate to increase the distance to the sample, a copper band maintains the electrical contact; <i>right</i> : side view.	40
6.16	<i>top</i> : Model of the setup with a sample prepared for etching; <i>bottom</i> : a sample after etching.	40

6.17	Comparison of a sample before (<i>top</i>) and after (<i>bottom</i>) etching.	41
6.18	SEM picture of a Fe_2VAl film with a thickness of $0.5\ \mu\text{m}$ on an unpolished silicon substrate.	42
6.19	SEM image of a $\text{Fe}_2\text{V}_{0.8}\text{W}_{0.2}\text{Al}$ film after etching.	42
7.1	Four-point measurement configuration.	44
7.2	Equivalent circuit diagram of a substrate-film system.	45
8.1	Four-point measurement of a bulk sample for measuring resistivity and Seebeck coefficient.	47
8.2	Four-point measurement of a thin film. The film is mounted on an insulator. Graphite strips between film and connectors cater for good electrical contact.	47
9.1	XRD-patterns of four samples of $(\text{Fe}_{2/3}\text{V}_{1/3})_{75+x}\text{Al}_{25-x}$ compounds. The positions of the expected Heusler peaks are shown at the bottom.	50
9.2	Thermoelectric properties of $(\text{Fe}_{2/3}\text{V}_{1/3})_{75+x}\text{Al}_{25-x}$ bulk samples.	51
9.3	Resistivity data of undoped and p-doped silicon wafers, which were produced using the Czochralski method. The wafers were annealed for seven days at $450\ ^\circ\text{C}$	53
9.4	Si Wafers.	53
9.5	SEM measurement of an unpolished undoped silicon wafer.	54
9.6	Resistivity and Seebeck measurements of $(\text{Fe}_{2/3}\text{V}_{1/3})_{72}\text{Al}_{28}$ thin films on silicon substrates after annealing for seven days at $450\ ^\circ\text{C}$	56
9.7	Electrical resistivity of a $0.5\ \mu\text{m}$ $\text{Fe}_2\text{V}_{0.8}\text{W}_{0.2}\text{Al}$ film before and after annealing and after removing the film.	58
9.8	Seebeck coefficient of a $0.5\ \mu\text{m}$ $\text{Fe}_2\text{V}_{0.8}\text{W}_{0.2}\text{Al}$ film before and after annealing and after removing the film.	59
9.9	Power Factor of a $0.5\ \mu\text{m}$ $\text{Fe}_2\text{V}_{0.8}\text{W}_{0.2}\text{Al}$ film before and after annealing and after removing the film.	59
9.10	(a): Electrical resistivity of various Al-films on silicon substrates before annealing; (b): Electrical resistivity of various Al-films on silicon substrates after annealing at $450\ ^\circ\text{C}$ for seven days.	60
9.11	(a): Seebeck coefficient of various Al-films on silicon substrates before annealing; (b): Seebeck coefficient of various Al-films on silicon substrates after annealing at $450\ ^\circ\text{C}$ for seven days.	61
9.12	(a): Electrical resistivity of a $0.05\ \mu\text{m}$ Al-films on a silicon substrate after annealing and 2 min etching; (b): Seebeck coefficient of a $0.05\ \mu\text{m}$ Al-films on a silicon substrate after annealing and 2 min etching.	61
9.13	Resistivity measurements of Chromium films with varying thicknesses on silicon substrates.	62

9.14	Seebeck measurements of Chromium films with varying thicknesses on silicon substrates.	63
9.15	(a): Resistivity measurements of not annealed 0.5 μm and 1 μm Fe_2VAI films on silicon substrates; (b): Seebeck measurements of not annealed 0.5 μm and 1 μm Fe_2VAI films on silicon substrates.	65
9.16	(a): Resistivity measurements of 0.5 μm Fe_2VAI films on silicon substrates before and after annealing; (b): Seebeck measurements of 0.5 μm Fe_2VAI films on silicon substrates before and after annealing.	65
9.17	(a): Resistivity measurements of 1 μm Fe_2VAI films on silicon substrates before and after annealing; (b): Seebeck measurements of 1 μm Fe_2VAI films on silicon substrates before and after annealing.	66
9.18	Resistivity contributions of a Si substrate and a 1 μm Fe_2VAI film, calculated from the measured data in figures 9.16a and 9.16b.	66

A Data Processing

```

1 import os
  import re
3
5 DELIMITER = "\t"
7 def analysiere_daten(filename):
    daten = []
9    header = []
    string = ''
11   f = open(filename, 'r')
    flag = True
13   flag2 = True
15   #read data from file and parse
    for line in f:
17       if flag == True and flag2 == True:
            header = line.split('\r')
19            header = header[0].split('\t')
            header = [x.strip() for x in header]
21            flag = False
        elif flag2 == True:
23            flag2 = False
            continue
25        else:
            temp = line.split('\t')
27            temp = [x.strip() for x in temp]
            try:
29                temp.remove('')
            except ValueError:
31                pass
            daten.append(temp)
33   f.close()
35   #manipulate data
    [r.pop(7) for r in daten]
37   [r.pop(6) for r in daten]
    [r.pop(3) for r in daten]
39   [r.pop(2) for r in daten]
41   for line in daten:
        line[0] = float(line[0]) + 273.15
43        line[1] = float(line[1]) * 10**8
        line[2] = float(line[2]) * 10**6
45        line[3] = float(line[3]) * 10**3

```

```
47     header2 = ["Measurement temp.(K)", "Resistivity(uOhm cm)", "Seebeck
coeff.(uV/K)", "Power factor(mW/m K^2)"]
    daten.insert(0, header2)

49
    #write data to file
51     if len(daten) < 6:
        for i in range(6 - len(daten)):
53         daten.append(['']*4)
    for i in range(len(daten)):
55         try:
            string += header[i] + DELIMITER
57         except IndexError:
            string += DELIMITER
59         for j in range(4):
            string += str(daten[i][j]) + DELIMITER
61         string += '\n'

63     g = open(filename[:-7] + "ausgewertet.txt", 'w')
    g.write(string)
65     g.close()

67
if __name__ == '__main__':
69     for filename in os.listdir('.'):
        if re.search('ana.txt', filename) is not None:
71         analysiere_daten(filename)

    appendix/analysiere_daten.py
```

B Intensity Distribution

Sputtering Intensity Distribution

```
In[*]:= Clear["`*"]
```

Geometric Dimensions

Target ring radius, distance target-substrate, substrate length and width in mm

```
In[*]:= rTarget = 10;  
d = 10;  
lenSubX = 25;  
lenSubY = 20;
```

Target Displacement from midpoint

```
In[*]:= xTarget = lenSubX / 2;  
yTarget = 0;
```

Calculate Intensity

Calculate distribution as a function of angle, Intensity at center of Target and normed Intensity

```
In[*]:= distribution[Phi_, x_, y_] :=  
      
$$\frac{d^4}{(d^2 + (x - xTarget - rTarget * Cos[Phi])^2 + (y - yTarget - rTarget * Sin[Phi])^2)^2}$$
;  
norm = NIntegrate[distribution[u, xTarget, yTarget], {u, 0, 2 Pi}];  
intensity[x_, y_] := NIntegrate[distribution[u, x, y], {u, 0, 2 Pi}] / norm;
```

Calculate Percentage

Area Dimensions in mm

```
In[*]:= x1 = -10;  
x2 = 10;  
y1 = -10;  
y2 = 10;
```

Integration Boundaries

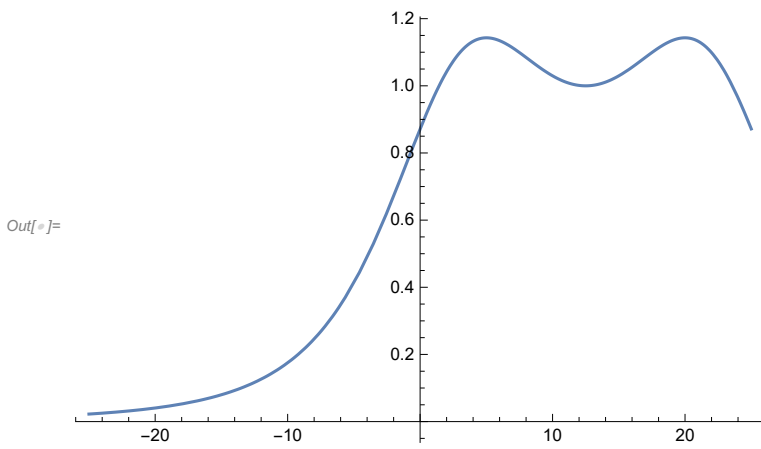
```
In[*]:= normbound = 1000;
```

Percentage of particles reaching defined area

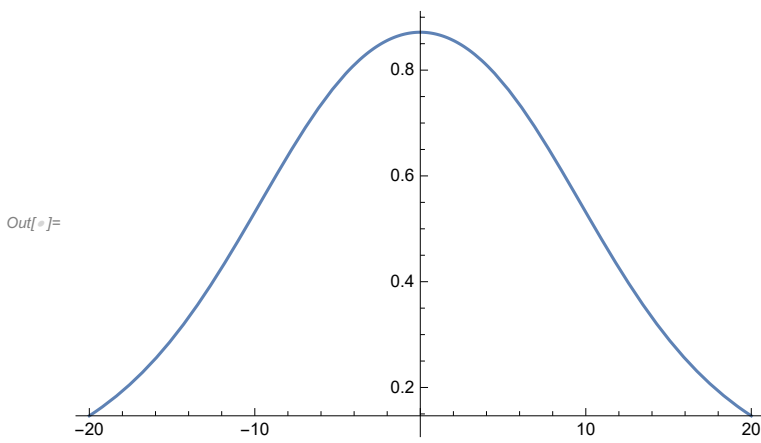
```
In[*]:= Quiet[total = NIntegrate[intensity[x, y],  
      {x, -normbound, normbound}, {y, -normbound, normbound}];  
percentage[g1_, g2_, g3_, g4_] := NIntegrate[intensity[x, y] / total,  
      {x, g1, g2}, {y, g3, g4}];
```

Plots

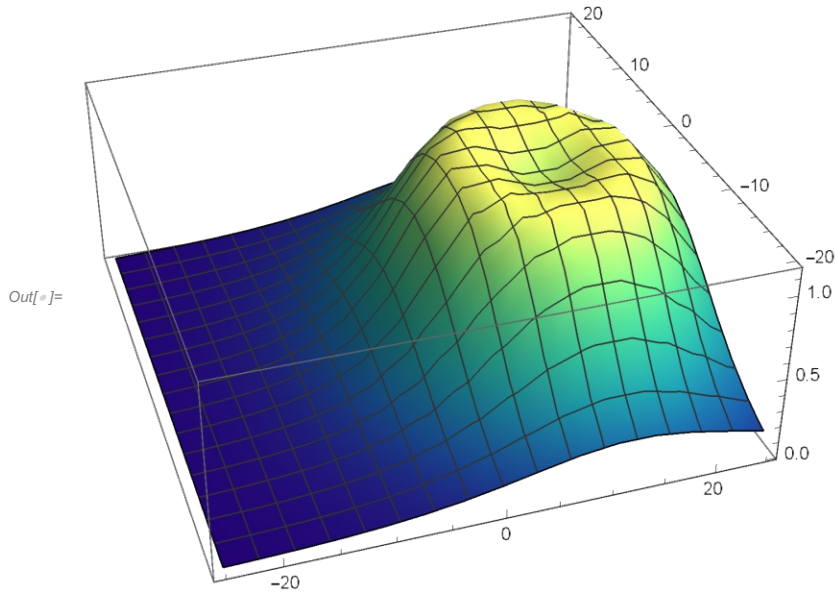
`In[]:= Plot[intensity[x, 0], {x, -lenSubX, lenSubX}]`



`In[]:= Plot[intensity[0, y], {y, -lenSubY, lenSubY}]`



```
In[ ]:= Plot3D[intensity[x, y], {x, -lenSubX, lenSubX},
  {y, -lenSubY, lenSubY}, ColorFunction -> "BlueGreenYellow"]
```



Percentage

```
In[ ]:= Quiet[PercentForm[percentage [-lenSubX/2, lenSubX/2, -lenSubY/2, lenSubY/2]]]
```

Out[]//PercentForm=
27.31%

C XRF-Evaluation

```

1 import PyPDF2
  import re
3 import openpyxl
  import os
5
  def change_concentration(path, output):
7     #read pdf from path
      filepath = path
9     with open(filepath, mode='rb') as f:
        reader = PyPDF2.PdfFileReader(f)
11        page = reader.getPage(0)
        txt = page.extractText()
13
        #find regex elements write to elements
15        match = re.findall("(\\D\\D?)(\\d*,...)(\\d*.,.*)", txt)
        elements = []
17        for i in range(len(match)):
            elements.append([match[i][0], float(match[i][1].replace(",","."))
19        ])
        name = re.findall("sample (.*)", txt)[0]
21
        data = berechnung(elements)
        convert2txt(name, data)
23
        #open excel
25        wb = openpyxl.load_workbook(filename='Teilchenprozent_Rechnung.xlsx')
        ws1 = wb['Tabelle1']
27        column = ws1['E']
        ws1['D2'].value = name
29        for i in range(len(column)):
            if i >= 6:
31                column[i].value = ""
33
        for line in ws1:
            for ele in elements:
35                if line[2].value == ele[0]:
                    line[4].value = ele[1]
37                print(ele[1])
39
        wb.save(output + ".xlsx")
41 def berechnung(gewichtsprozent):
43     massen = {"Fe":55.845,
               "V": 50.942,
```

```

45     "Al": 26.982,
        "W": 183.84,
47     "Cr": 51.996,
        "O": 15.999,
49     "Si": 28.085,
        "Ga": 69.723,
51     "Ta": 180.95,
        "Mn": 54.938,
53     "Ti": 47.867,
        "Co": 58.933}

55
gewichtsprozent_ele = [row[0] for row in gewichtsprozent]
gewichtsprozent_mass = [row[1] for row in gewichtsprozent]
normierte_gewichtsprozent = [x/sum(gewichtsprozent_mass)*100. for x
in gewichtsprozent_mass]
59 teilchenprozent = []
    for i in range(len(normierte_gewichtsprozent)):
61         teilchenprozent.append(normierte_gewichtsprozent[i] / massen.get(
gewichtsprozent_ele[i]))
        normierte_teilchenprozent = [x/sum(teilchenprozent)*100. for x in
teilchenprozent]
63 verbindung = [x/100.*4. for x in normierte_teilchenprozent]
fe_norm = []
65 index_fe = gewichtsprozent_ele.index('Fe')
    for i in range(len(verbindung)):
67         fe_norm.append(verbindung[i]/verbindung[index_fe]*2)

69     txt = "Element\tGew%\tNorm. Gew.  %\tTeilchen  %\tNorm. Teil %\
\tVerbindung\tAuf Fe norm.\n"
        for i in range(len(fe_norm)):
71             txt += str(gewichtsprozent_ele[i]) + "\t" + '{:06.3f}'.format(
gewichtsprozent_mass[i]) + "\t" + '{:06.3f}'.format(
normierte_gewichtsprozent[i]) + "\t\t" + '{:04.2f}'.format(
teilchenprozent[i]) + "\t\t" + '{:05.2f}'.format(
normierte_teilchenprozent[i]) + "\t\t" + '{:04.2f}'.format(
verbindung[i]) + "\t\t" + '{:04.2f}'.format(fe_norm[i]) + "\n"
            print(txt)
73     return(txt)

75 def convert2txt(name, txt):
    try:
77         f = open("Quantification " + name + ".txt", "w")
    except IOError:
79         f = open("Quantification_of_unreadable_sample.txt", "w")
        f.write(name + "\n\n")
81         f.write(txt)
        f.close()

```

83

```
85 if __name__ == '__main__':
    pdf_files = []
87     directory = os.listdir(".")
    for file in directory:
89         match = re.findall("Quantification.*.pdf", file)
        if match != []:
91             pdf_files.append(match[0])
    print(pdf_files)
93
    for i in pdf_files:
95         change_concentration(i, i)

                                appendix/teilchenprozent.py
```